The Astrophysical Journal, 976:93 (23pp), 2024 November 20 https://doi.org/10.3847/1538-4357/ad82de
© 2024. The Author(s). Published by the American Astronomical Society.
OPEN ACCESS

# A SPectroscopic Survey of Biased Halos In the Reionization Era (ASPIRE): JWST Supports Earlier Reionization around [O III] Emitters

Xiangyu Jin[1], Jinyi Yang[1,2], Xiaohui Fan[1], Feige Wang[1,2], Koki Kakiichi[3], Romain A. Meyer[4], George D. Becker[5], Siwei Zou[6,7], Eduardo Bañados[8], Jaclyn B. Champagne[1], Valentina D'Odorico[9,10,11], Minghao Yue[12], Sarah E. I. Bosman[8,13], Zheng Cai[7], Anna-Christina Eilers[12], Joseph F. Hennawi[14,15], Hyunsung D. Jun[16,17], Mingyu Li[7], Zihao Li[3,7], Weizhe Liu (刘伟哲)[1], Maria Pudoka[1], Sindhu Satyavolu[18], Fengwu Sun[1,19], Wei Leong Tee[1], and Yunjing Wu[7]

[1] Steward Observatory, University of Arizona, 933 N. Cherry Ave., Tucson, AZ 85721, USA
[2] Department of Astronomy, University of Michigan, 1085 S. University Ave., Ann Arbor, MI 48109, USA
[3] Cosmic Dawn Center (DAWN), Niels Bohr Institute, University of Copenhagen, Jagtvej 128, København N, DK-2200, Denmark
[4] Department of Astronomy, University of Geneva, Chemin Pegasi 51, 1290 Versoix, Switzerland
[5] Department of Physics & Astronomy, University of California, Riverside, CA 92521, USA
[6] Chinese Academy of Sciences South America Center for Astronomy, National Astronomical Observatories, CAS, Beijing 100101, People's Republic of China
[7] Department of Astronomy, Tsinghua University, Beijing 100084, People's Republic of China
[8] Max Planck Institut für Astronomie, Königstuhl 17, D-69117 Heidelberg, Germany
[9] INAF—Osservatorio Astronomico, via G.B. Tiepolo, 11, I-34143 Trieste, Italy
[10] Scuola Normale Superiore, Piazza dei Cavalieri, I-56126 Pisa, Italy
[11] IFPU—Institute for Fundamental Physics of the Universe, via Beirut 2, I-34151 Trieste, Italy
[12] MIT Kavli Institute for Astrophysics and Space Research, 77 Massachusetts Ave., Cambridge, MA 02139, USA
[13] Institut für Theoretische Physik, Universität Heidelberg, Philosophenweg 16, D-69120 Heidelberg, Germany
[14] Department of Physics, Broida Hall, University of California, Santa Barbara, CA 93106-9530, USA
[15] Leiden Observatory, Leiden University, P.O. Box 9513, NL-2300 RA Leiden, The Netherlands
[16] Department of Physics, Northwestern College, 101 7th St. SW, Orange City, IA 51041, USA
[17] SNU Astronomy Research Center, Seoul National University, 1 Gwanak-ro, Gwanak-gu, Seoul 08826, Republic of Korea
[18] Tata Institute of Fundamental Research, Homi Bhabha Rd., Mumbai 400005, India
[19] Center for Astrophysics | Harvard & Smithsonian, 60 Garden St., Cambridge, MA 02138, USA
*Received 2024 June 13; revised 2024 September 12; accepted 2024 October 1; published 2024 November 14*

## Abstract

Understanding when and how reionization happened is crucial for studying the early structure formation and the properties of the first galaxies in the Universe. At $z > 5.5$, the observed intergalactic medium (IGM) optical depth shows a significant scatter, indicating an inhomogeneous reionization process. However, the nature of the inhomogeneous reionization remains debated. A SPectroscopic survey of biased halos In the Reionization Era (ASPIRE) is a JWST Cycle 1 program that has spectroscopically identified >400 [O III] emitters in 25 quasar fields at $z > 6.5$. Combined with deep ground-based optical spectroscopy of ASPIRE quasars, the ASPIRE program provides the current largest sample for IGM-galaxy connection studies during cosmic reionization. We present the first results of IGM effective optical depth measurements around [O III] emitters using 14 ASPIRE quasar fields. We find the IGM transmission is tightly related to reionization era galaxies to the extent that a significant excess of Ly$\alpha$ transmission exists around [O III] emitters. We measure the stacked IGM effective optical depth of IGM patches associated with [O III] emitters and find they reach the same IGM effective optical depth at least $dz \sim 0.1$ ahead of those IGM patches where no [O III] emitters are detected, supporting earlier reionization around [O III] emitters. Our results indicate an enhancement in IGM Ly$\alpha$ transmission around [O III] emitters at scales beyond 25 $h^{-1}$ cMpc, consistent with the predicted topology of reionization from fluctuating UV background models.

*Unified Astronomy Thesaurus concepts:* Reionization (1383); High-redshift galaxies (734); Intergalactic medium (813); Quasar absorption line spectroscopy (1317)

## 1. Introduction

Cosmic reionization was the last major phase transition of atomic hydrogen from neutral to ionized in the intergalactic medium (IGM). During cosmic reionization, ionized regions, created and powered by UV bright sources, gradually grew and overlapped in the IGM. Understanding when and how reionization happened not only reveals properties of the first luminous sources in the Universe, but also provides crucial information on the early structure formation and large-scale structure in the early Universe (S. L. Finkelstein et al. 2019; B. E. Robertson 2022).

Observations have revealed that reionization ended at $z < 6$ through various astrophysical sources. The Thomson scattering optical depth observed from cosmic microwave background observations implies a midpoint of reionization around $z \sim 7.7$ (Planck Collaboration et al. 2020). At $z \gtrsim 6$, IGM Ly$\alpha$ damping wing profiles—strong absorption caused by significantly neutral gas—are widely observed among luminous quasars (e.g., B. Greig et al. 2017, 2019, 2022, 2024; E. Bañados et al. 2018; F. B. Davies et al. 2018b; F. Wang et al. 2020; J. Yang et al. 2020a; D. Ďurovčíková et al. 2024), in galaxies (A. J. Bunker et al. 2023; H. Umeda et al. 2023, but see K. E. Heintz et al. 2023; L. C. Keating et al. 2023; K. E. Heintz et al. 2024), and in

Original content from this work may be used under the terms of the Creative Commons Attribution 4.0 licence. Any further distribution of this work must maintain attribution to the author(s) and the title of the work, journal citation and DOI.

gamma-ray burst afterglows (T. Totani et al. 2016, but see O. E. Hartoog et al. 2015). The discovery of Gunn–Peterson troughs, where the observed flux in the Ly$\alpha$ forest is consistent with zero, is smoking gun evidence for an ongoing reionization at $z\sim6$ (J. E. Gunn & B. A. Peterson 1965; R. H. Becker et al. 2001). At $z<6$, prominent transmission spikes, as opposed to the dark absorption troughs, are emergent in the Ly$\alpha$ forest (I. D. McGreer et al. 2011, 2015; Y. Zhu et al. 2021, 2022; X. Jin et al. 2023).

Meanwhile, the Ly$\alpha$ visibility of galaxies increases rapidly from $z>6$ to $z<6$ (e.g., D. P. Stark et al. 2010, 2011; J. Caruana et al. 2014; L. Pentericci et al. 2014; M. A. Schenker et al. 2014; S. De Barros et al. 2017; C. A. Mason et al. 2018, 2019). Those observations support a rapid evolution in the IGM neutral fraction at $6<z<8$. Accumulating observational evidence shows that reionization might still be ongoing at $z<6$ (for a review, see X. Fan et al. 2023), including recent ionizing photon mean free path measurements showing a dramatic evolution at $5<z<6$ (G. D. Becker et al. 2021; Y. Zhu et al. 2023), the existence of dark regions in both quasar Ly$\alpha$ and Ly$\beta$ forests at $z<6$ (Y. Zhu et al. 2021, 2022; X. Jin et al. 2023), detections of damping wing absorption in the Ly$\alpha$ forest at $z<6$ (G. D. Becker et al. 2024; B. Spina et al. 2024; Y. Zhu et al. 2024), and the large scatter in the observed IGM effective optical depth ($\tau_{\rm eff}$) distribution at $z\gtrsim5.4$, which cannot be explained by homogeneous ionizing background models (J. Yang et al. 2020b; S. E. I. Bosman et al. 2022).

At $z\sim5.5$, although $\tau_{\rm eff}$ measured from Ly$\alpha$ forests suggests the IGM is highly ionized with an average neutral fraction $\lesssim10^{-4}$, the observed $\tau_{\rm eff}$ distribution (usually measured in a bin size of $50\,h^{-1}$ cMpc), displays an increased scatter at $z>5.5$ (X. Fan et al. 2006; G. D. Becker et al. 2015; S. E. I. Bosman et al. 2018, 2022; A.-C. Eilers et al. 2018; J. Yang et al. 2020b). The scatter in $\tau_{\rm eff}$ at $z>5.5$ reflects large-scale variations close to the end of reionization and implies a patchy and inhomogeneous reionization process. X. Fan et al. (2006) propose that the large scatter is driven by the fluctuations in the UV ionizing background (UVB), while A. Lidz et al. (2006) argue that the scatter could be explained by density field fluctuations with a uniform ionizing background. A. D'Aloisio et al. (2015) suggest that variations in the IGM temperature can also explain the observed fluctuation in $\tau_{\rm eff}$. These reionization models predict distinct topologies of reionization to the extent of the relation between the density field and large-scale IGM transmission. In the fluctuating UVB models, overdense regions of galaxies correspond to enhancement in the IGM transmission because galaxies enhance the ionizing radiation field around them (F. B. Davies & S. R. Furlanetto 2016; F. B. Davies et al. 2018a, 2024). On the other hand, if large-scale fluctuations are driven by density field or IGM temperature, overdense regions in the IGM correspond to the suppression of IGM transmission (e.g., F. B. Davies et al. 2018a).

Previous observational studies have investigated the relation between galaxies and IGM transmission using ground-based observations. G. D. Becker et al. (2018), H. M. Christenson et al. (2021), R. Ishimoto et al. (2022), and H. M. Christenson et al. (2023) have utilized Hyper-Suprime Cam on the Subaru Telescope to select Ly$\alpha$ emitters (LAEs) at $z\sim5.7$ and have investigated the relation between the surface number density of LAEs and $\tau_{\rm eff}$ using a few quasar sightlines. Significant underdensity of LAEs has been found around a few highly opaque IGM patches at $z\sim5.7$ (G. D. Becker et al. 2018; H. M. Christenson et al. 2021), consistent with the fluctuating UVB models. Using broadband selected Lyman-break galaxies (LBGs), D. Kashino et al. (2020) find an underdensity of LBGs at $5.5<z<5.9$ along the long dark trough at $z\sim5.7$ exhibited in the quasar J0148 + 0600, also consistent with fluctuating UVB models. However, for highly transparent quasar sightlines, both overdensities (R. Ishimoto et al. 2022) and underdensities (H. M. Christenson et al. 2023) of LAEs have been found, which may be in tension with either fluctuating UVB or IGM temperature models. As addressed in H. M. Christenson et al. (2023), at lower redshift, LAEs are found to avoid high-density peaks in the IGM (e.g., N. Kashikawa et al. 2007; R. Momose et al. 2021; Y. Huang et al. 2022) because Ly$\alpha$ emission can be suppressed in high density of neutral gas (Y. Huang et al. 2022, see also M. Tang et al. 2024), or star formation activity is quenched by the strong ionizing background in the high-density regions (N. Kashikawa et al. 2007; T. S. Lambert et al. 2024). Therefore, other tracers of the density field are needed. In addition, K. Kakiichi et al. (2018) and R. A. Meyer et al. (2019, 2020) measure the cross-correlation function between the quasar Ly$\alpha$ forest spectrum and various galaxy populations, including LBGs, faint galaxies traced by C IV absorbers, and LAEs identified in the quasar field, and find excess IGM transmission with $\sim3\sigma$ at $\gtrsim10$ cMpc, suggesting enhanced IGM transmission is associated with galaxies. However, selecting high-redshift galaxies with ground-based observations is expensive and the number of galaxies identified in the quasar fields is also limited, resulting in difficulty of detecting significant signals in the IGM-galaxy cross-correlation function. It is thus preferred to use space-based observations to select enough high-redshift galaxies in quasar fields and investigate the relation between IGM transmission and galaxies in a statistical manner.

The James Webb Space Telescope (JWST) has revolutionized the identification of high-redshift galaxies by detecting their rest-optical emission lines. Utilizing JWST NIRCam Wide-field Slitless Spectroscopy (WFSS) mode, the Emission-line galaxies and Intergalactic Gas in the Epoch of Reionization (EIGER) program (PID-1243) targets six quasar fields at $6.0<z<7.1$. D. Kashino et al. (2023) identify 117 [O III] emitters in one quasar field at $z\sim6.3$ from the EIGER program, and measure the IGM-galaxy cross-correlation function based on 59 [O III] emitters located within the Ly$\alpha$ and Ly$\beta$ forests. A SPectroscopic survey of biased halos In the Reionization Era (ASPIRE; PID-2078) is a program that targets 25 quasar fields at $6.5<z<6.8$. Along with ground-based spectroscopy covering the quasar Ly$\alpha$ forest, ASPIRE provides the current largest sample of quasar fields for studying the connection between galaxies and IGM during the reionization era. In this paper, we investigate the relation between galaxies and IGM transmission in a statistical manner, utilizing 14 ASPIRE quasar fields. This paper is organized as follows: In Section 2, we introduce the data reduction of JWST WFSS data, the selection of [O III] emitters, and the data reduction of ground-based optical spectroscopy. In Section 3, we introduce the method to quantify the IGM transmission around [O III] emitters. We show the stacked IGM transmission around [O III] emitters in Section 4. In Section 5, we investigate the $\tau_{\rm eff}$ distribution around [O III] emitters at different redshifts and on various scales. We summarize the paper in Section 6. Throughout this paper, we adopt a flat $\Lambda$CDM cosmology

**Table 1**
Summary of ASPIRE Quasars Used in This Work

| Quasar Name | Quasar Redshift | No. of O3Es | Telescope/Instrument | Exposure Time (hr) | References | $\tau_{\rm lim,2\sigma}$ ($z = 6.0$) |
|---|---|---|---|---|---|---|
| (1) | (2) | (3) | (4) | (5) | (6) | (7) |
| J0109−3047 | 6.7909 | 23 | VLT/X-SHOOTER | 6.0 | J. Yang et al. (2020b) | 4.60 |
| J0218+0007 | 6.77 | 31 | Gemini/GMOS | 4.0 | New data | 4.72 |
| J0224−4711 | 6.5222 | 17 | VLT/X-SHOOTER | 8.6 | V. D'Odorico et al. (2023) | 6.32 |
| J0226+0302 | 6.5412 | 34 | VLT/X-SHOOTER | 6.5 | V. D'Odorico et al. (2023) | 6.65 |
| J0244−5008 | 6.724 | 32 | Magellan/LDSS3 | 2.3 | New data | 5.79 |
| J0305−3150 | 6.6145 | 50 | VLT/X-SHOOTER | 4.0 | J. Yang et al. (2020b) | 5.02 |
| J0525−2406 | 6.5397 | 14 | Gemini/GMOS | 2.7 | New data | 3.70 |
| J1048−0109 | 6.6759 | 18 | VLT/X-SHOOTER | 1.3 | J. Yang et al. (2020b) | 4.48 |
| J1104+2134 | 6.7662 | 8 | Keck/LRIS | 2.0 | J. Yang et al. (2020b) | 5.78 |
| J1129+1846 | 6.823 | 5 | VLT/X-SHOOTER | 4.5 | E. Bañados et al. (2021) | 5.48 |
| J1526−2050 | 6.5864 | 20 | VLT/X-SHOOTER | 12.2 | V. D'Odorico et al. (2023) | 6.52 |
| J2002−3013 | 6.6876 | 12 | Gemini/GMOS | 2.3 | J. Yang et al. (2020b) | 5.49 |
| J2102−1458 | 6.648 | 10 | Keck/DEIMOS | 3.3 | J. Yang et al. (2020b) | 4.91 |
| J2232+2930 | 6.666 | 13 | VLT/X-SHOOTER | 4.0 | J. Yang et al. (2020b) | 5.53 |

**Note.** (1) Quasar name, in the ascending order of R.A; (2) quasar spectroscopic redshift; (3) number of $5.4 < z < 7.0$ [O III] emitters identified in the quasar fields; (4) telescope and instrument of the optical spectroscopy; (5) exposure time in hours (hr); (6) reference of the optical spectroscopy reduction; (7) $2\sigma$ limiting optical depth, calculated in a $50\,h^{-1}$ cMpc centered bin at $z \sim 6.0$.

with cosmological parameters $H_0 = 70\,{\rm km\,s^{-1}\,Mpc^{-1}}$ and $\Omega_m = 0.3$.

## 2. Data Preparation

To probe the connection between galaxies and IGM, we use data from ASPIRE program (PI: F. Wang) to select galaxies in the quasar fields through [O III] doublet emission lines. We present ground-based optical spectroscopy covering the Ly$\alpha$ forest of ASPIRE quasars to measure the IGM Ly$\alpha$ transmission. In this section, we summarize the data reduction details of JWST NIRCam observations and ground-based optical spectroscopy.

### 2.1. JWST NIRCam/WFSS Observations from the ASPIRE Program

ASPIRE is a program that targets 25 quasar fields at $6.5 < z < 6.8$ with NIRCam Imaging and WFSS (M. J. Rieke et al. 2005; T. P. Greene et al. 2017). The WFSS mode enables efficient identification of reionization era galaxies through their rest-optical emission lines (e.g., F. Sun et al. 2022). An overview of the ASPIRE program can be found in F. Wang et al. (2023) and J. Yang et al. (2023), and we briefly summarize it below. In each quasar field, the F356W WFSS observations in the long-wavelength channel were taken simultaneously with the F200W imaging in the short-wavelength channel with a total on-source time of 2834.5 s. Imaging (includes direct imaging and out-of-field imaging) in F115W and F356W were taken in each quasar field with a total exposure time from 1417.3 s near the quasar to 472.4 s at the edge of the field. There is a single pointing in each quasar field and the target quasar is designed to be located at Module A with an X offset of $-60\farcs5$ and a Y offset of $7\farcs5$. We refer readers to F. Wang et al. (2023) and J. Yang et al. (2023) for more details about the data reduction.

Using ASPIRE program, H$\beta$ and [O III] emission lines of $z \sim 5.4$–$7.0$ galaxies can be identified by F356W WFSS data (e.g., F. Wang et al. 2023; J. Yang et al. 2023; Y. Wu et al. 2023; S. Zou et al. 2024; J. Champagne et al. 2024a, 2024b). We follow the procedure in F. Wang et al. (2023) to search for [O III] emitters. We first extract the 1D spectrum from WFSS data and place a median filter of 51 pixels on the spectrum. We perform a peak finding on the extracted spectrum to search the emission lines with $>5\sigma$ detection. To search [O III] emitters, we then assume the detected emission line is [O III]$\lambda$5008 and search the spectra with [O III]$\lambda$4960 with $>2\sigma$ detection. Those selected line emitters are viewed as [O III] emitter candidates. We then perform a visual inspection on all [O III] emitter candidates and remove those that are likely selected due to source confusion and contaminant line emitters at low redshift. More details regarding the detection of line emitters and identification of [O III] emitters can be found in F. Wang et al. (2024, in preparation).

### 2.2. Ground-based Optical Spectroscopy

To measure the transmission in quasar Ly$\alpha$ forests, we utilize existing ground-based optical spectroscopy (J. Yang et al. 2020b; V. D'Odorico et al. 2023) of ASPIRE quasars, and collect new optical spectroscopy of ASPIRE quasars. Overall, we are able to analyze 14 ASPIRE quasar sightlines given by the currently available data. Broad absorption line quasars are not included in the analysis. We present details of these optical spectroscopy in the following subsections, and summarize the optical observations and number of [O III] emitters identified in quasar fields in Table 1.

#### 2.2.1. Archival Optical Spectroscopy

J0224−4711 and J1526−2050 are included in the ESO Large Program the Ultimate X-SHOOTER Legacy Survey of Quasars at the Reionization Epoch (XQR-30) (PI: V. D'Odorico) and J0226+0302 is included as part of an enlarged XQR-30 sample (E-XQR-30, V. D'Odorico et al. 2023). X-SHOOTER is an Echelle spectrograph on the Very Large Telescope (VLT) with a wavelength coverage of 300–2500 nm covered by three arms: UVB, VIS, and near-IR. In the optical band covered by the VIS arm, X-SHOOTER achieves a spectral resolution $R$ of ∼8800 with a $0\farcs9$ slit

(J. Vernet et al. 2011). We downloaded the E-XQR-30 reduced optical spectra from the GitHub repository.[20] The reduced E-XQR-30 spectra are rebinned to 10 km s$^{-1}$.

In addition, we collect reduced archival optical spectroscopy of J0109−3047, J0305−3150, J0910+1656, J1048−0109, J1104+2134, J2002−3013, J2102−1458, and J2232+2930 from J. Yang et al. (2020b), and J1129+1846 from E. Bañados et al. (2021). J0109−3047, J0305−3150, J1048−0109, J1129+1846, and J2232+2930 were observed with VLT/X-SHOOTER. J1104+2134 was observed with Keck/LRIS (J. B. Oke et al. 1995; C. Rockosi et al. 2010), with a 600/10,000 grating and a 1″ slit, resulting in a spectral resolution of $R\sim1900$. J2002−3013 was observed with the Gemini/GMOS-S with the R400 grating and a 0.″5 slit (I. M. Hook et al. 2004; G. Gimeno et al. 2016), with a spectral resolution of $R\sim1900$. J2102−1458 was observed with Keck/DEIMOS with the 830G grating and a 1″ slit (S. M. Faber et al. 2003), resulting in a spectral resolution of $R\sim3300$. We refer readers to J. Yang et al. (2020b) for more data reduction details.

#### 2.2.2. New Optical Spectroscopy

Apart from archival data, we also include new optical spectroscopy from 6 to 10 m telescopes. J0218+0007 and J0525−2406 were observed in the Gemini/GMOS-S queues with R400 with a central wavelength of 855 nm and 860 nm in 2019 with the R400 grating and a spectral resolution of $R\sim1900$ (PI: J. Yang). J0244−5008 was observed with Magellan Clay/LDSS3 with VPH-Red (grism) with a 1″ slit (PI: M. Yue). The central wavelength is 8000 Å and the spectral resolution is $R\sim1800$.

For the new optical spectroscopy, we use `PypeIt` v.1.14.0 (J. Prochaska et al. 2020a; J. X. Prochaska et al. 2020b) to perform data reduction for bias subtracting, flat-fielding, and flux calibration, following the standard procedure.[21]

For each quasar sightline, following J. Yang et al. (2020b), we exclude a rest-frame wavelength range <1040 Å in the Ly$\alpha$ forest to remove the contamination from Ly$\beta$ and O VI emission lines. We also exclude the Ly$\alpha$ forest spectrum at rest wavelength >1176 Å to avoid possible emission from the quasar proximity zone. The redshift distribution of ASPIRE quasars used in this work and the redshift coverage of their Ly$\alpha$ forest are shown in Figure 1. Following J. Yang et al. (2020b) and X. Jin et al. (2023), we use the least-squares method to fit the spectrum within the rest frame 1245–1285 Å and 1310–1380 Å by assuming a broken power law with a break at 1000 Å (J. M. Shull et al. 2012). The quasar intrinsic continuum flux is calculated using the best-fit power-law continuum. Transmitted flux in the Ly$\alpha$ forest ($T_{\rm Ly\alpha}$) is then calculated as the normalized flux $T_{\rm Ly\alpha}=F_{\rm obs}/F_{\rm cont}$, where $F_{\rm obs}$ is the observed flux in the Ly$\alpha$ forest and $F_{\rm cont}$ is the flux of the best-fit power-law continuum at the same wavelength. To remove the contamination from strong sky emission lines to IGM transmission, following X. Jin et al. (2023), we mask pixels likely influenced by strong sky emission lines.

As the depth of the optical spectroscopy varies by quasar sightlines, we measure the $2\sigma$ limiting optical depth $\tau_{\rm lim,2\sigma}$ of each quasar sightline to quantify the depth of the optical spectroscopy. A higher $\tau_{\rm lim,2\sigma}$ indicates the quasar spectrum can detect weaker IGM transmission. We adopt the formula

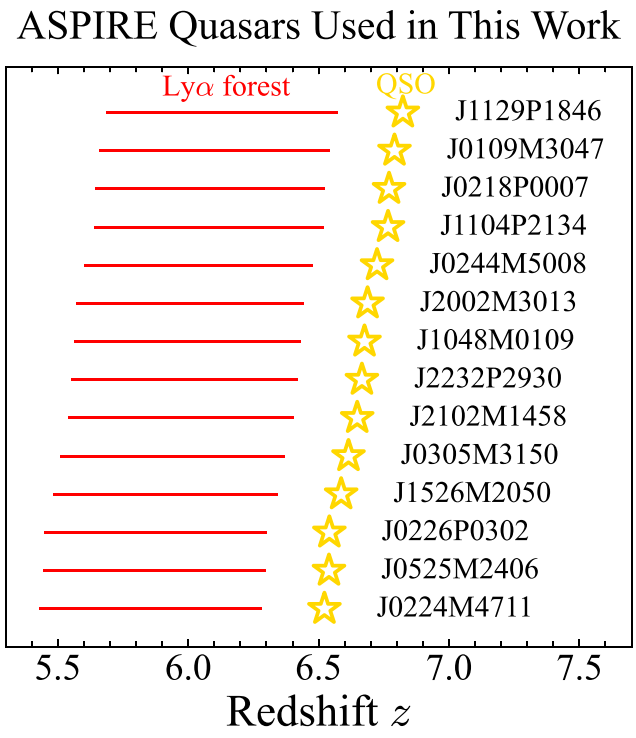


**Figure 1.** The redshift distribution (yellow) of ASPIRE quasars used in this work, in the ascending order of redshift, and the redshift range of the Ly$\alpha$ forest used in the analysis is denoted by the red horizontal line. We exclude the Ly$\alpha$ forest spectrum at >1176 Å rest frame to exclude the possible emission from the quasar proximity zone and exclude the rest $\lambda<1040$ Å Ly$\alpha$ forest to exclude the contamination from O VI$\lambda$ 1033 emission and the Ly$\beta$ forest. The redshift range of ASPIRE quasars used in this work is from $z\sim6.5$ to $z\sim6.8$ and the corresponding Ly$\alpha$ absorption redshift range is from $z\sim5.4$ up to $z\sim6.6$.

$\tau_{\rm lim,2\sigma}=-\ln\langle 2\sigma/F_{\rm cont}\rangle$ to calculate $\tau_{\rm lim,2\sigma}$, where $\sigma$ is the spectral uncertainty, and $F_{\rm cont}$ is the continuum flux calculated from the best-fit power-law continuum described above. The $\tau_{\rm lim,2\sigma}$ is measured within a $50\,h^{-1}$ cMpc bin centered at $z=6.0$, and the $\tau_{\rm lim,2\sigma}$ at $z\sim6$ of 14 quasar sightlines used in this work is ∼3.7–6.7. Out of 14 ASPIRE quasars, one-third of the quasar sightlines with the highest signal-to-noise ratio (S/N) and the corresponding IGM-galaxy cross-correlation function will be presented in K. Kakiichi et al. (2024, in preparation).

## 3. Methods

### 3.1. IGM Ly$\alpha$ $\tau_{eff}$ Measurements

Because the spectral resolution and the exposure time of optical spectroscopy vary, we use a large bin size to measure the IGM transmission through $\tau_{\rm eff}$ measurements. We first measure $\tau_{\rm eff}$ of each individual quasar sightline, defined as $\tau_{\rm eff}=-\ln\langle T_{\rm Ly\alpha}\rangle$, where $T_{\rm Ly\alpha}$ is the transmitted flux in the Ly$\alpha$ forest mentioned in Section 2. We follow G. D. Becker et al. (2015), A.-C. Eilers et al. (2018), S. E. I. Bosman et al. (2018, 2022), and J. Yang et al. (2020b), adopting a bin size of $50\,h^{-1}$ cMpc, and measure $\tau_{\rm eff}$ in $50\,h^{-1}$ cMpc bins, starting from the rest frame 1040 Å up to the rest frame 1176 Å. If the transmitted flux is not detected in a $50\,h^{-1}$ cMpc bin (i.e., $\langle T_{\rm Ly\alpha}\rangle<\langle 2\sigma/F_{\rm continuum}\rangle$), in this case, we use $\tau_{\rm lim,2\sigma}$ as the $2\sigma$ lower limit of $\tau_{\rm eff}$.

[20] https://github.com/XQR-30/Spectra
[21] https://pypeit.readthedocs.io/en/release/cookbook.html

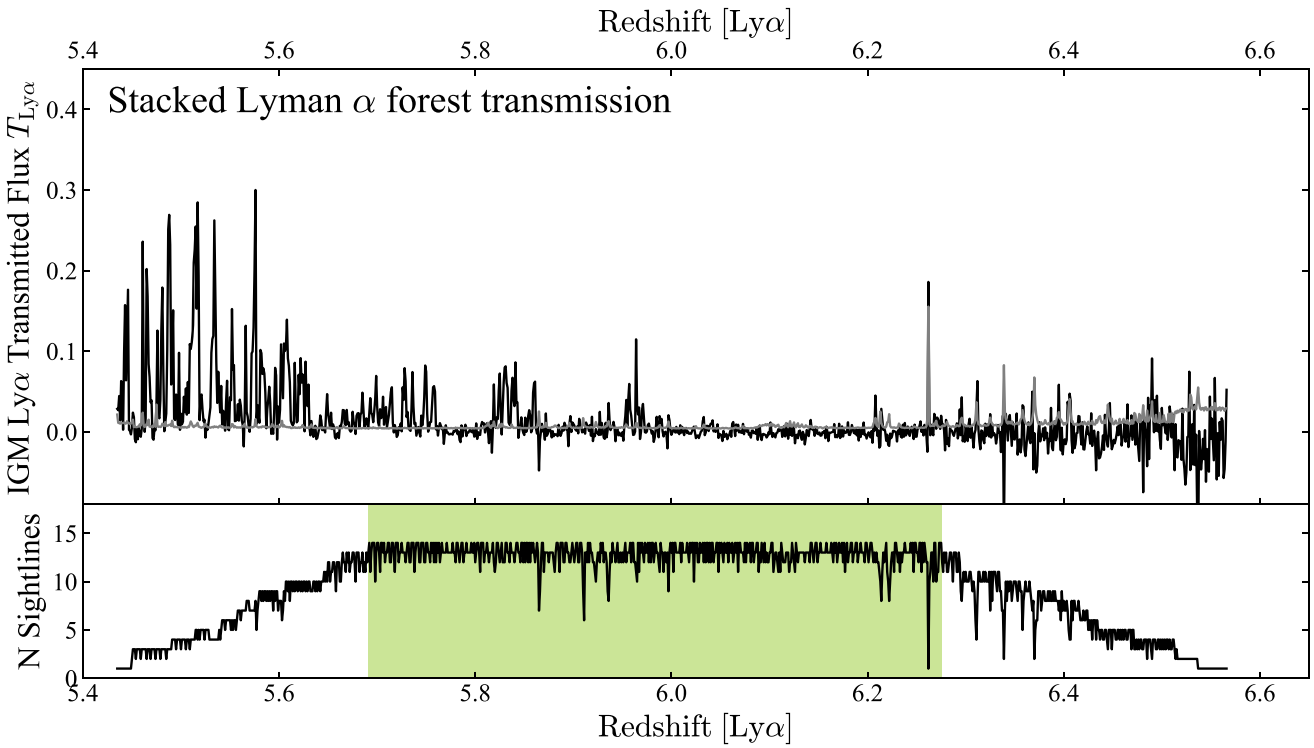


**Figure 2.** Top—The stacked Ly$\alpha$ forest spectrum (black) of 14 ASPIRE quasar sightlines used in our analysis, adopting a redshift grid of $dz = 0.001$ from $z = 5.435$ to $z = 6.568$. The spectral uncertainty of the stacked spectrum is shown in gray. Bottom—The number of quasar lines of sight (LOSs) available in each pixel of the redshift grid. Nearly all quasars used in this work cover the $z \sim 5.70-6.27$ Ly$\alpha$ forest (the green-shaded region). Some pixels are strongly influenced by sky OH emission lines, therefore, they have been removed in the analysis, resulting in troughs shown in the number of quasar LOSs.

To examine the overall $\tau_{\rm eff}$ distribution of 14 ASPIRE quasar sightlines, we stack their Ly$\alpha$ forest spectrum. As the spectral resolution of different instruments varies, we use a common redshift grid with $dz = 0.001$ to stack the Ly$\alpha$ forest spectrum, adopting inverse variance weighting to avoid contamination from sky emission-line residuals. The spectral uncertainty of the stacked spectrum is also calculated using the inverse variance weighting. The inverse variance used for weighting has been normalized by the quasar continuum flux at the corresponding rest wavelength. The stacked Ly$\alpha$ forest spectrum is shown in the top panel of Figure 2. The bottom panel of Figure 2 shows the number of quasar sightlines available at each redshift grid. Nearly all quasar sightlines used in this work cover a Ly$\alpha$ absorption redshift range of $z \sim 5.70$–$6.27$. We then measure the $\tau_{\rm eff}$ of the stacked Ly$\alpha$ forest spectrum in $50\,h^{-1}$ cMpc bins, starting from $z \sim 5.47$ up to $z \sim 6.48$.

Figure 3 shows $\tau_{\rm eff}$ of 14 individual quasar sightlines and $\tau_{\rm eff}$ of the stacked Ly$\alpha$ forest spectrum (i.e., Figure 2). The $\tau_{\rm eff}$ measurements for the single sightlines show a rapid increase and a large scatter as the trend observed in the previous works at $z > 5.5$ (X. Fan et al. 2006; G. D. Becker et al. 2015; S. E. I. Bosman et al. 2018, 2022; A.-C. Eilers et al. 2018; J. Yang et al. 2020b). We show the best-fit $\tau_{\rm eff}$ redshift evolution from J. Yang et al. (2020b) and S. E. I. Bosman et al. (2022). The best-fit $\tau_{\rm eff}$ redshift evolution from J. Yang et al. (2020b) displays a higher $\tau_{\rm eff}$ than S. E. I. Bosman et al. (2022) at the same redshift. S. E. I. Bosman et al. (2022) argue that this difference could be attributed to the cosmic variance of the different quasar samples as well as to the different quasar continuum reconstruction methods. J. Yang et al. (2020b) adopt a broken power law to calculate the quasar continuum flux, while S. E. I. Bosman et al. (2022) use principal component analysis. S. E. I. Bosman et al. (2021) suggest the power-law continuum reconstruction has a mean bias of 9.58% over the Ly$\alpha$ forest because it does not fit broad emission lines, but it can accurately recover the continuum emission between broad emission lines. In this work, we analyze the quasar rest-frame wavelength range of 1040–1176 Å, which does not include broad emission lines such as Ly$\beta$ and O VI. Therefore, the power-law continuum should not introduce significant biases to the $\tau_{\rm eff}$ calculation. The $\tau_{\rm eff}$ of the stacked Ly$\alpha$ forest transmission of 14 ASPIRE quasars falls between the best-fit $\tau_{\rm eff}$ redshift evolution derived from J. Yang et al. (2020b) and S. E. I. Bosman et al. (2022) at $z < 6.1$, and at $z > 6.1$, the stacked $\tau_{\rm eff}$ are lower limits. The $\tau_{\rm eff}$ distribution shown in Figure 3 provides a baseline for IGM Ly$\alpha$ transmission, against which the IGM Ly$\alpha$ transmission around [O III] emitters will be evaluated.

### 3.2. Measuring the IGM Lyα Transmission around [O III] Emitters

With [O III] emitters selected by JWST NIRCam WFSS observations, it is now possible to study the connection between IGM transmission and galaxies. The top panel of Figure 4 shows the transmitted spectrum of an ASPIRE quasar J0226+0302, together with the spatial location of all [O III] emitters identified in the same quasar field. The transmitted spectrum of all 14 ASPIRE quasars used in this work can be found in Appendix A. The spatial locations of [O III] emitters are denoted by the [O III] redshift $z_{\rm [O\,III]}$ of the identified [O III]

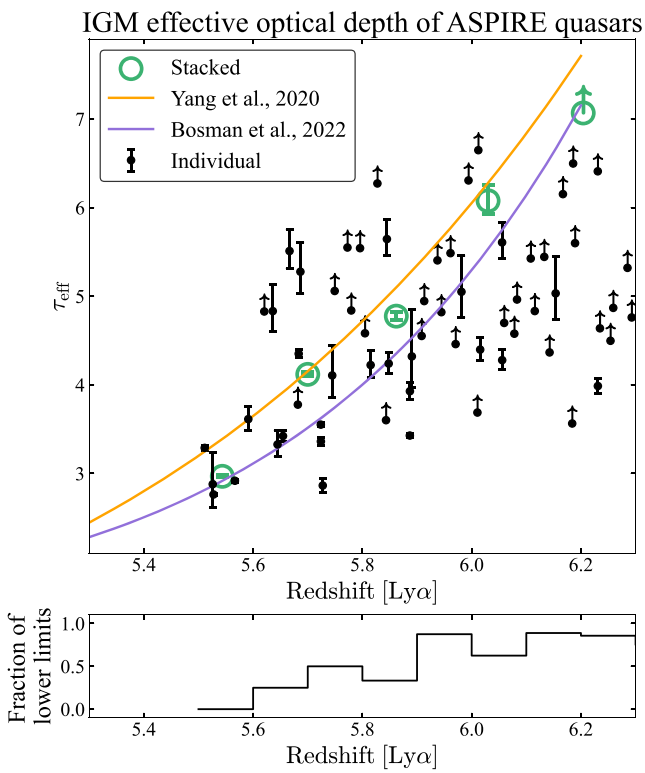


**Figure 3.** Top—The IGM Ly$\alpha$ effective optical depth $\tau_{\rm eff}$ of 14 ASPIRE quasar sightlines used in this work and the $\tau_{\rm eff}$ of the stacked Ly$\alpha$ forest spectrum in a bin size of 50 $h^{-1}$ cMpc. All the lower limits in the $\tau_{\rm eff}$ are shown by upward arrows. As a comparison, we show the best-fit $\tau_{\rm eff}$ redshift evolution from J. Yang et al. (2020b, orange) and S. E. I. Bosman et al. (2022, purple), derived from larger samples of 32 quasars and 67 quasars. Bottom—The fraction of $2\sigma$ lower limits in the $\tau_{\rm eff}$ measurements within a redshift bin of $dz = 0.1$. Beyond $z \sim 6.1$, more than 75% of measurements are $2\sigma$ lower limits.

emitter and the transverse distance $r_\perp$ between the [O III] emitter and the quasar.

To probe the connection between IGM transmission and galaxies, we put a sphere centered at the detected [O III] emitters with a certain radius (hereafter "influence radius"). If the sphere intersects the Ly$\alpha$ forest, we then measure $\tau_{\rm eff}$ over the path length enclosed by the sphere (the bottom panel of Figure 4). For [O III] emitters whose sphere does not intersect the Ly$\alpha$ forest, we then regard that those [O III] emitters are too distant to influence the quasar Ly$\alpha$ forest. For [O III] emitters close to the boundary of the Ly$\alpha$ forest included in our analysis, we only use the path length enclosed by the sphere and within the Ly$\alpha$ forest to measure $\tau_{\rm eff}$. By measuring $\tau_{\rm eff}$ around [O III] emitters, we sample the IGM transmission around them. As such, the resulting $\tau_{\rm eff}$ distribution will be a biased distribution, including the galaxy proximity effect.

We first adopt an influence radius of 25 $h^{-1}$ cMpc and then measure the $\tau_{\rm eff}$ around [O III] emitters (hereafter $\tau_{\rm eff,[O\ III]}$). In this case, twice the influence radius is equal to 50 $h^{-1}$ cMpc, which is the bin size used for $\tau_{\rm eff}$ measurements in Figure 3. We show the dependence of $\tau_{\rm eff,[O\ III]}$ integrated length on the transverse distance $r_\perp$ in the left panel of Figure 5. Because all detected [O III] emitters in ASPIRE fields have $r_\perp \ll 50\,h^{-1}$ cMpc, for most $\tau_{\rm eff,[O\ III]}$ measurements, by adopting an influence radius of 25 $h^{-1}$ cMpc, the corresponding integrated path length is $\sim$49−50 $h^{-1}$ cMpc, except for those [O III] emitters close to the boundary of the Ly$\alpha$ forest (i.e., $z_{\rm [O\ III]}<5.7$ or $z_{\rm [O\ III]}>6.3$). This ensures that most $\tau_{\rm eff,[O\ III]}$ is measured with a nearly uniform integrated length of $\sim$50 $h^{-1}$ cMpc as $\tau_{\rm eff}$ measurements in Figure 3. We show $\tau_{\rm eff,[O\ III]}$ as a function of the [O III] emitter redshift $z_{\rm [O\ III]}$ in the right panel of Figure 5. If the IGM Ly$\alpha$ transmission is not detected ($<2\sigma$)around an [O III] emitter, we then use $\tau_{\rm lim,2\sigma}$ as the $2\sigma$ lower limit of $\tau_{\rm eff,[O\ III]}$. Similar to the redshift evolution of $\tau_{\rm eff}$ shown in Figure 3, $\tau_{\rm eff,[O\ III]}$ around individual [O III] emitters also shows an increasing trend as the redshift increases and displays a large scatter. Because the integrated length is shorter for $z \lesssim 5.7$ $\tau_{\rm eff,[O\ III]}$ measurements, the scatter in $\tau_{\rm eff,[O\ III]}$ is larger at $z \lesssim 5.7$ than at $z \gtrsim 5.7$, reflecting small-scale variations in IGM transmission. At $z \gtrsim 5.7$, the redshift evolution of $\tau_{\rm eff,[O\ III]}$ displays a slightly flatter trend than the redshift evolution of $\tau_{\rm eff}$ denoted by the orange line in the right panel of Figure 5. At $z > 6$, most $\tau_{\rm eff,[O\ III]}$ measurements are lower limits due to the depth of the current data.

## 4. IGM Patches Are More Transparent around [O III] Emitters

We first investigate $\tau_{\rm eff}$ of the stacked Ly$\alpha$ forest spectrum centered at [O III] emitters using an influence radius of 25 $h^{-1}$ cMpc used in Figure 5. By adopting a certain influence radius, for the Ly$\alpha$ forest spectrum of each quasar sightline, we split the Ly$\alpha$ forest spectrum into two parts: (1) the Ly$\alpha$ forest spectrum centered at [O III] emitters (i.e., the part of Ly$\alpha$ forest spectrum that intersects the sphere of [O III] emitters); and (2) the Ly$\alpha$ forest spectrum away from [O III] emitters, where no [O III] emitters are detected (i.e., the part of Ly$\alpha$ forest spectrum that does not intersect the sphere of any detected [O III] emitters). We then stack the Ly$\alpha$ forest spectrum centered at [O III] emitters and the Ly$\alpha$ forest spectrum away from [O III] emitters separately, using the inverse variance weighting and the same redshift grid as Figure 2. The top panel of Figure 6 shows the stacked spectrum of the Ly$\alpha$ forest spectrum around [O III] emitters and away from [O III] emitters, and the bottom panel of Figure 6 shows the number of quasar sightlines in each pixel.

By comparing the stacked entire Ly$\alpha$ forest spectrum (Figure 2) and stacked Ly$\alpha$ forest spectrum centered at [O III] emitters (the red line in the top panel of Figure 6), the majority of the Ly$\alpha$ transmission in the stacked entire Ly$\alpha$ forest spectrum is around [O III] emitters (within an influence radius of 25 $h^{-1}$ cMpc). Compared with the stacked Ly$\alpha$ forest spectrum away from [O III] emitters, the stacked Ly$\alpha$ forest spectrum centered at [O III] emitters displays more prominent IGM transmission at $z > 5.7$. To test whether the result is mainly caused by the bias toward high S/N quasar sightlines, we generate the stacked Ly$\alpha$ transmission spectrum using the unweighted average transmission. The unweighted average Ly$\alpha$ transmission centered at [O III] emitters and away from [O III] emitters is shown in the middle panel of Figure 6. Compared with the stacked Ly$\alpha$ transmission calculated by the inverse variance weighting, the unweighted average Ly$\alpha$ transmission shows more pixel-to-pixel variations, but a smoother evolution in redshift. The unweighted average Ly$\alpha$ transmission around [O III] emitters is still more prominent than the unweighted average Ly$\alpha$ transmission away from [O III] emitters at the same redshift. This suggests that regions traced by [O III] emitters are playing important roles in contributing to the local ionizing background and producing the observed transmission in the Ly$\alpha$ forest.

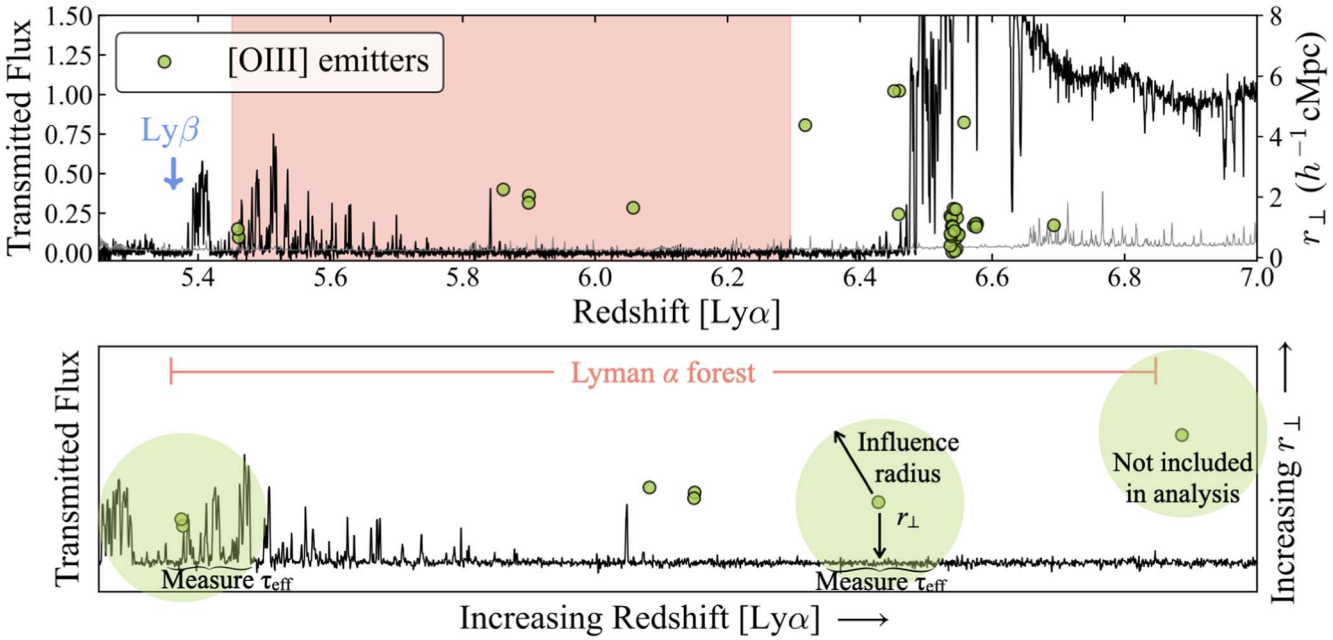


**Figure 4.** Top—The transmitted spectrum of an ASPIRE quasar J0226+0302. The redshift range of the Ly$\alpha$ used in the analysis is displayed in the red-shaded region. The location of the Ly$\beta$ emission line is marked by the blue downward arrow. The spatial locations of the [O III] emitters identified in each quasar field are denoted by the yellow-green-filled circles in terms of the [O III] emitter redshift $z_{\rm [O\ III]}$ and the transverse distance $r_\perp$ between the [O III] emitter and the central quasar. Bottom—An illustrative figure for measuring the IGM transmission around the [O III] emitters within the Ly$\alpha$ forest of J0226+0302. For each [O III] emitter identified in the quasar field, we put a sphere of a certain radius ("influence radius") centered at the [O III] emitter. For better visualization, we only show the spheres of three [O III] emitters and the size of the sphere is only for illustrative purposes, not to scale. For an [O III] emitter of which the sphere intersects the Ly$\alpha$ forest, we assume that the [O III] emitter is able to "influence" the Ly$\alpha$ forest.

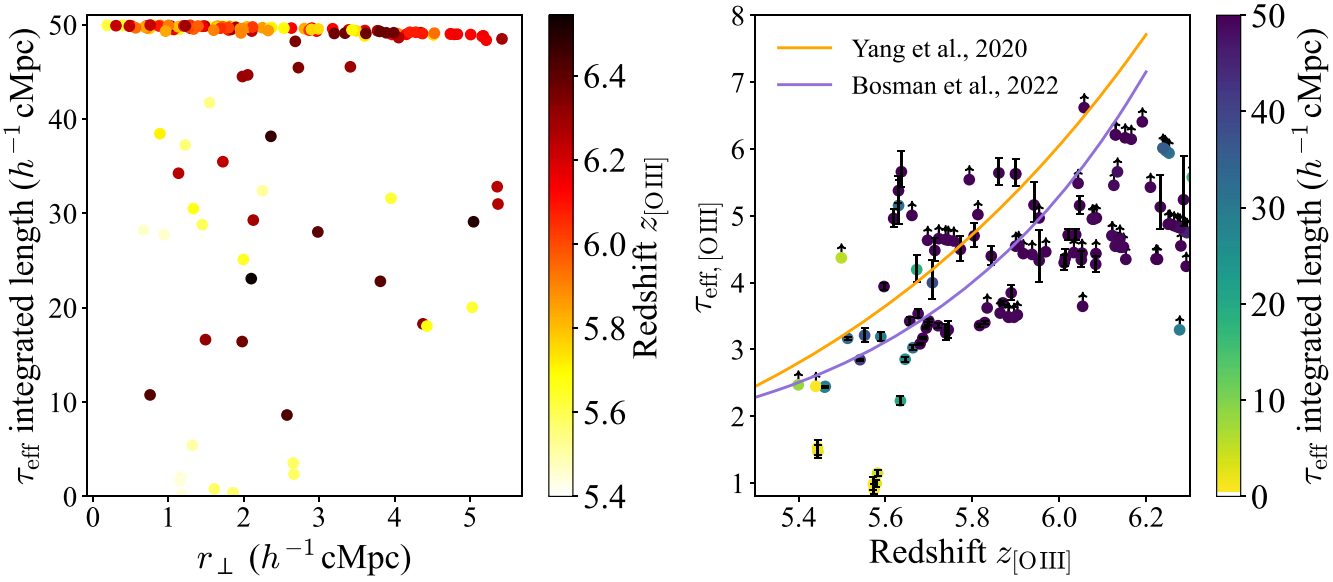


**Figure 5.** Left—The integrated path length for $\tau_{\rm eff,\ [O\ III]}$ measurements as a function of the transverse distance ($r_\perp$), adopting an influence radius of 25 $h^{-1}$ cMpc. Each point is color-coded by the redshift of the [O III] emitter $z_{\rm [O\ III]}$. Except for those [O III] emitters at the boundary of the Ly$\alpha$ forest, for most [O III] emitters, the integrated length for $\tau_{\rm eff,\ [O\ III]}$ measurements is $\sim$50 $h^{-1}$ cMpc. Right—The $\tau_{\rm eff}$ around the [O III] emitters ($\tau_{\rm eff,\ [O\ III]}$) adopting an influence radius of 25 $h^{-1}$ cMpc, as the function of the [O III] emitter redshift $z_{\rm [O\ III]}$. The integrated path length for each $\tau_{\rm eff,\ [O\ III]}$ measurement is color-coded. The best-fit $\tau_{\rm eff}$ redshift evolution from J. Yang et al. (2020b) and S. E. I. Bosman et al. (2022) is denoted by the orange and purple lines, respectively.

We then measure the $\tau_{\rm eff}$ of stacked Ly$\alpha$ transmission spectra centered at and away from [O III] emitters (the top panel of Figure 6). We show the $\tau_{\rm eff}$ measurements in Figure 7 by the red hollow square markers (centered at [O III] emitters) and the blue hollow hexagon markers (away from [O III] emitters). The $\tau_{\rm eff}$ of the stacked Ly$\alpha$ forest spectrum centered at [O III] emitters is significantly ($>5\sigma$) lower than the $\tau_{\rm eff}$ of the stacked Ly$\alpha$ forest spectrum away from [O III] emitters. At the same redshift, the IGM patches away from [O III] emitters have an average $\tau_{\rm eff}$ of $\gtrsim$0.5 higher than the $\tau_{\rm eff}$ of the IGM patches around [O III] emitters, suggesting that near [O III] emitters, the IGM patches are more transparent than those regions in the IGM where no [O III] emitters are detected. This indicates a higher IGM transmission near [O III] emitters and suggests that [O III] emitters can enhance the ionizing radiation field around them, resulting in a higher local ionizing background. This

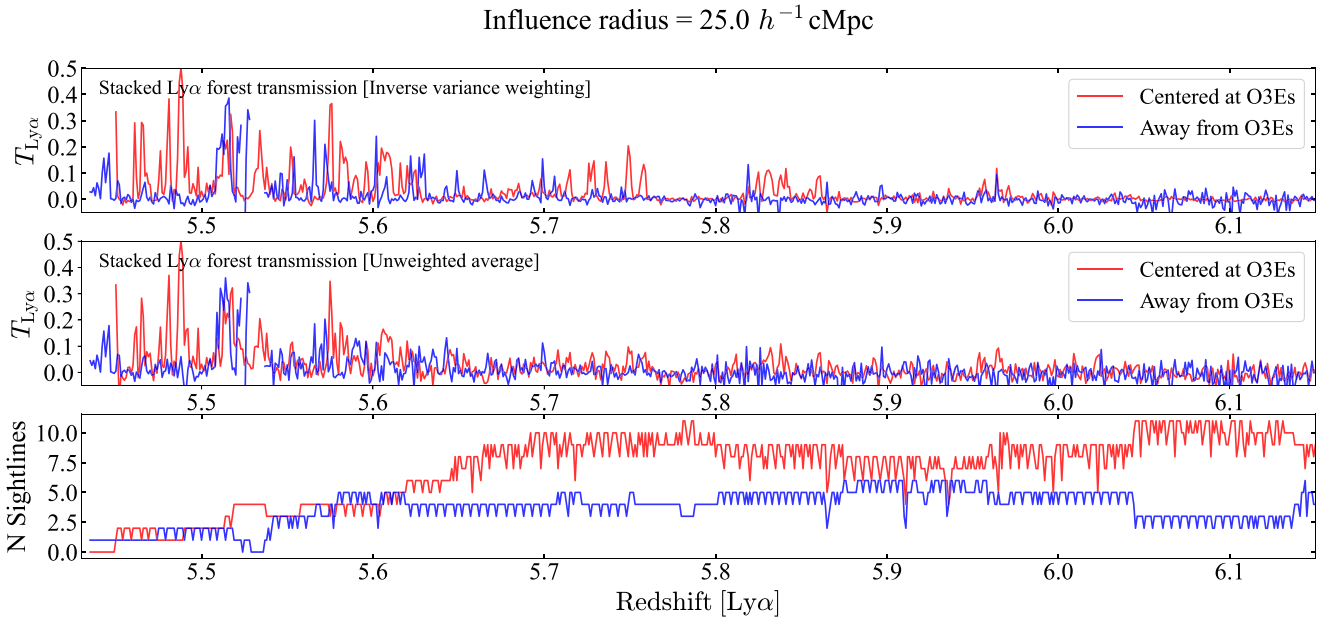


**Figure 6.** Top—The stacked transmission of the Ly$\alpha$ forest around [O III] emitters (red) and away from [O III] emitters (blue), adopting the inverse variance weighting and an influence radius of 25 $h^{-1}$ cMpc; see the text for details. Middle—The stacked transmission of the Ly$\alpha$ forest around [O III] emitters (red) and away from [O III] emitters (blue), where the stacked transmission is the unweighted average transmission. Bottom—The number of quasar LOSs available in each pixel of the stacked Ly$\alpha$ forest transmission around [O III] emitters (red) and the stacked Ly$\alpha$ forest transmission away from [O III] emitters (blue).

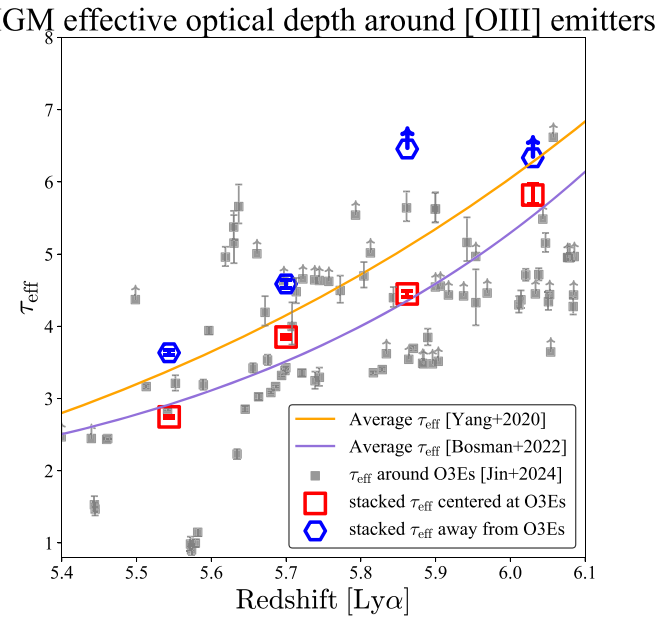


**Figure 7.** The $\tau_{\rm eff}$ measurements of the stacked Ly$\alpha$ forest spectrum centered at [O III] emitters (the red line in the top panel of Figure 6) are denoted by red open squares, and the $\tau_{\rm eff}$ measurements of the stacked Ly$\alpha$ forest spectrum away from [O III] emitters (the blue line in the top panel of Figure 6) are marked by blue open hexagons. Individual measurements of IGM optical depth around [O III] emitters $\tau_{\rm eff,[O\ III]}$ are shown in filled gray squares, adopting an influence radius of 25 $h^{-1}$ cMpc. The best-fit redshift evolutions of $\tau_{\rm eff}$ from J. Yang et al. (2020b) and S. E. I. Bosman et al. (2022) are denoted by the orange and the purple lines, respectively.

implies the scatter in the observed $\tau_{\rm eff}$ at $z > 5.5$ is tightly associated with the fluctuations in the ionizing background (X. Fan et al. 2006; F. B. Davies et al. 2024). By comparing the same optical depth around [O III] emitters and away from [O III] emitters, we find the IGM patches around [O III] emitters reach the same $\tau_{\rm eff}$ around $dz \sim 0.1$ earlier than IGM patches where no [O III] emitters are detected, suggesting reionization processes faster ($\gtrsim$23 Myr ahead) around [O III] emitters before the end of reionization ($z \sim 5.3$) (S. E. I. Bosman et al. 2022).

## 5. Discussion

In this section, we examine the distribution of $\tau_{\rm eff}$ around [O III] emitters (i.e., $\tau_{\rm eff,[O\ III]}$) at different redshifts and on various scales, and investigate whether IGM patches around [O III] emitters are biased toward more transparent or more opaque IGM patches, thereby constraining the topology of reionization.

### 5.1. IGM Effective Optical Depth Distribution around z < 6.1 [O III] Emitters

Although all ASPIRE quasars used in this work cover a Ly$\alpha$ absorption redshift at $z > 6.1$, given the depth of the current data, >75% of measurements are 2$\sigma$ lower limits if we include $z > 6.1$ $\tau_{\rm eff}$ measurements (see Figure 3). Therefore, we only investigate the distribution of $\tau_{\rm eff,[O\ III]}$ at $z < 6.1$.

By adopting an influence radius of 25 $h^{-1}$ cMpc, most integrated lengths are close to the bin size (50 $h^{-1}$ cMpc) used in previous IGM $\tau_{\rm eff}$ studies (see G. D. Becker et al. 2015; S. E. I. Bosman et al. 2018; A.-C. Eilers et al. 2018; J. Yang et al. 2020b). We show the distribution of $\tau_{\rm eff,[O\ III]}$ around $z < 6.1$ [O III] emitters in a histogram in Figure 8(a). To compare the $\tau_{\rm eff,[O\ III]}$ distribution with the $\tau_{\rm eff}$ distribution measured in Section 3.1, we generate a random $\tau_{\rm eff,[O\ III]}$ distribution. We utilize the spatial location of $z < 6.1$ [O III] emitters detected in the other 13 quasar fields and recompute $\tau_{\rm eff,[O\ III]}$ for each quasar field, based on the methods described in Section 3. We show the random $\tau_{\rm eff,[O\ III]}$ distribution in a brown line in Figure 8(b). The random $\tau_{\rm eff,[O\ III]}$ distribution provides a control sample to compare with the $\tau_{\rm eff,[O\ III]}$

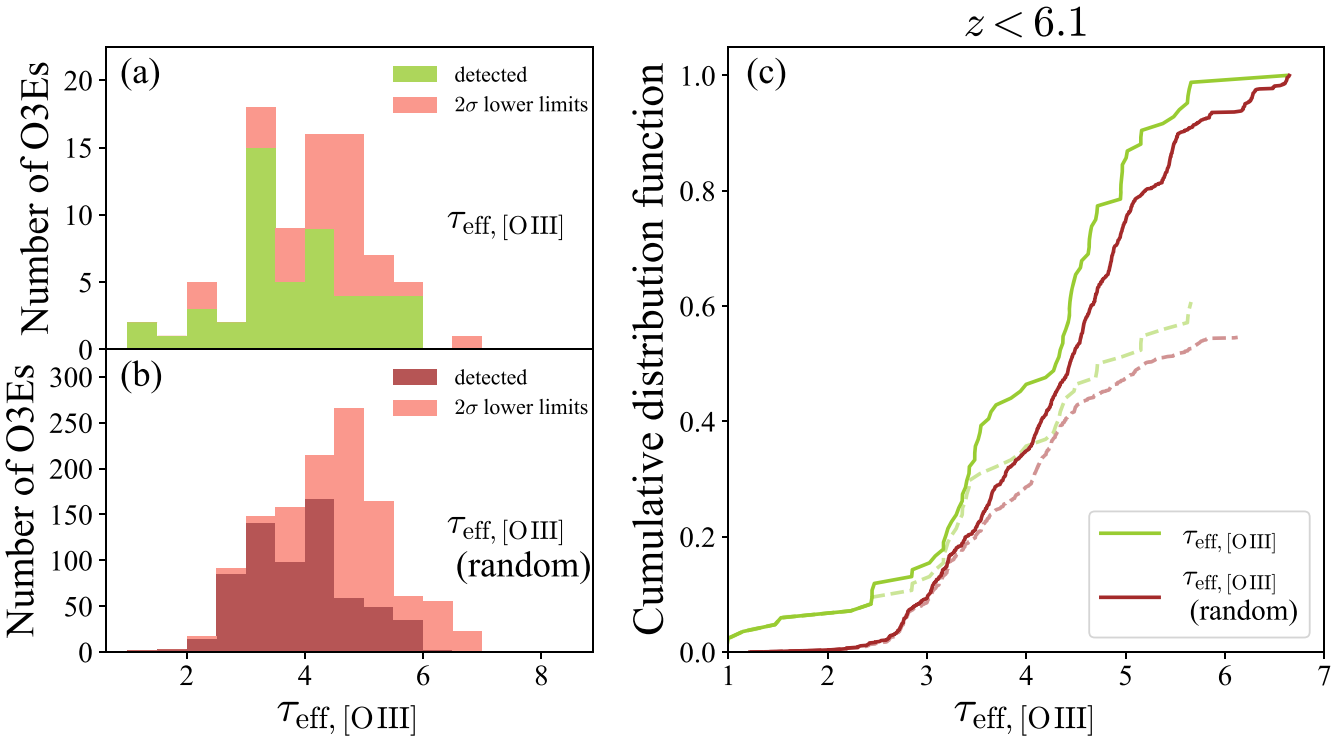


**Figure 8.** (a) The distribution of $\tau_{\rm eff}$ around the [O III] emitters ($\tau_{\rm eff,[O\ III]}$) by adopting an influence radius of 25 $h^{-1}$ cMpc. (b) The random distribution of $\tau_{\rm eff,[O\ III]}$ by adopting an influence radius of 25 $h^{-1}$ cMpc. The distributions of $2\sigma$ lower limits of $\tau_{\rm eff}$ are shown in red in (a) and (b). (c) The CDFs of the $\tau_{\rm eff,[O\ III]}$ (yellow-green) and the random distribution (brown). For $2\sigma$ lower limits of $\tau_{\rm eff}$, we plot them as actual measurements (solid line) or infinity (dashed line) in CDF.

distribution. Ideally, the random distribution can well represent the original $\tau_{\rm eff}$ distribution of IGM patches measured in Section 3.1. We compare the random $\tau_{\rm eff,[O\ III]}$ distribution with the original $\tau_{\rm eff}$ distribution of IGM patches in Appendix B, and find the random $\tau_{\rm eff,[O\ III]}$ distribution is consistent with the original $\tau_{\rm eff}$ distribution of IGM patches.

In Figures 8(a) and (b), the distribution of $2\sigma$ lower limits of $\tau_{\rm eff,[O\ III]}$ is shown in red. The distribution of $\tau_{\rm eff,[O\ III]}$ displays a more significant peak at a $\tau_{\rm eff}$ of $\sim$3 than the random distribution. In Figure 8(c), we show the cumulative distribution functions (CDFs) of the $\tau_{\rm eff,[O\ III]}$ distribution and the random $\tau_{\rm eff,[O\ III]}$ distribution. Because there are lower limits in both distributions, following S. E. I. Bosman et al. (2018, 2022), we treat the lower limits as either (1) the "optimistic" case: the transmitted flux is just below the $2\sigma$ detection limit (i.e., $\tau_{\rm eff} = \tau_{\rm lim,2\sigma}$) or (2) the "pessimistic" case: the intrinsic transmitted flux is zero (i.e., $\tau_{\rm eff} = \infty$ ). The CDFs of these two different cases are plotted in solid lines ($\tau_{\rm eff} = \tau_{\rm lim,2\sigma}$) and dashed lines ($\tau_{\rm eff} = \infty$ ) in Figure 8(c), respectively. The optimistic and pessimistic cases set the upper and lower bounds of the CDFs. The distribution of $\tau_{\rm eff,[O\ III]}$ displays a higher cumulative probability than the random distribution of $\tau_{\rm eff,[O\ III]}$ for both the optimistic and pessimistic cases.

In previous studies, the optimistic CDF is often adopted when examining whether two distributions are consistent (e.g., G. D. Becker et al. 2015; J. Yang et al. 2020b; S. E. I. Bosman et al. 2022), especially when comparing with those CDFs derived from simulations assuming homogeneous UVB models (e.g., S. E. I. Bosman et al. 2022). Because there are a number of lower limits (i.e., right-censored data) in the $\tau_{\rm eff,[O\ III]}$ distribution, we use the `lifelines` package (C. Davidson-Pilon 2019) to perform the log-rank test between the $\tau_{\rm eff,[O\ III]}$ distribution and the random distribution to examine whether they are drawn from the same parent distribution. The $p$-value for the null hypothesis is 0.0198, suggesting that the CDFs of $\tau_{\rm eff,[O\ III]}$ and random $\tau_{\rm eff,[O\ III]}$ are different ($>2\sigma$) when adopting an influence radius of 25 $h^{-1}$ cMpc.

Furthermore, we measure $\tau_{\rm eff,[O\ III]}$ of all $z < 6.1$ [O III] emitters and corresponding random $\tau_{\rm eff,[O\ III]}$ distributions by adopting different influence radii. We then investigate whether these two distributions will be significantly different at certain scales. Figure 9 shows the optimistic and pessimistic CDFs of $\tau_{\rm eff,[O\ III]}$ and the random distribution using influence radii from 5 $h^{-1}$ cMpc to 50 $h^{-1}$ cMpc to demonstrate two distinct methods for handling lower limits in the distribution function. When the data set includes censored data (i.e., lower limits or upper limits), survival analysis can be used to reconstruct the distribution function (E. D. Feigelson & P. I. Nelson 1985). For each distribution containing $2\sigma$ lower limits of $\tau_{\rm eff,[O\ III]}$, we use the Kaplan–Meier (KM) estimator, included in the `lifelines` package (C. Davidson-Pilon 2019), to fit the survival function. The $1\sigma$ confidence interval from the KM estimator of the fitted CDF is plotted as the shaded region in Figure 9. The null hypothesis $p$-value from the log-rank test is shown in the bottom right corner of each subpanel. With influence radii $\lesssim$20 $h^{-1}$ cMpc, the CDF of $\tau_{\rm eff,[O\ III]}$ distribution is consistent with the random $\tau_{\rm eff,[O\ III]}$ distribution with a $p$-value $>$0.05. When the influence radius is $\gtrsim$25 $h^{-1}$ cMpc, the CDF of $\tau_{\rm eff,[O\ III]}$ is significantly higher than the random $\tau_{\rm eff,[O\ III]}$ distribution at the same $\tau_{\rm eff,[O\ III]}$, with a null hypothesis $p$-value $<$0.05, indicating that around $z < 6.1$ [O III] emitters, the IGM patches are more transparent around [O III] emitters than elsewhere in the IGM on scales greater than 25 $h^{-1}$ cMpc, consistent with the topology of reionization predicted by the fluctuating UVB models.

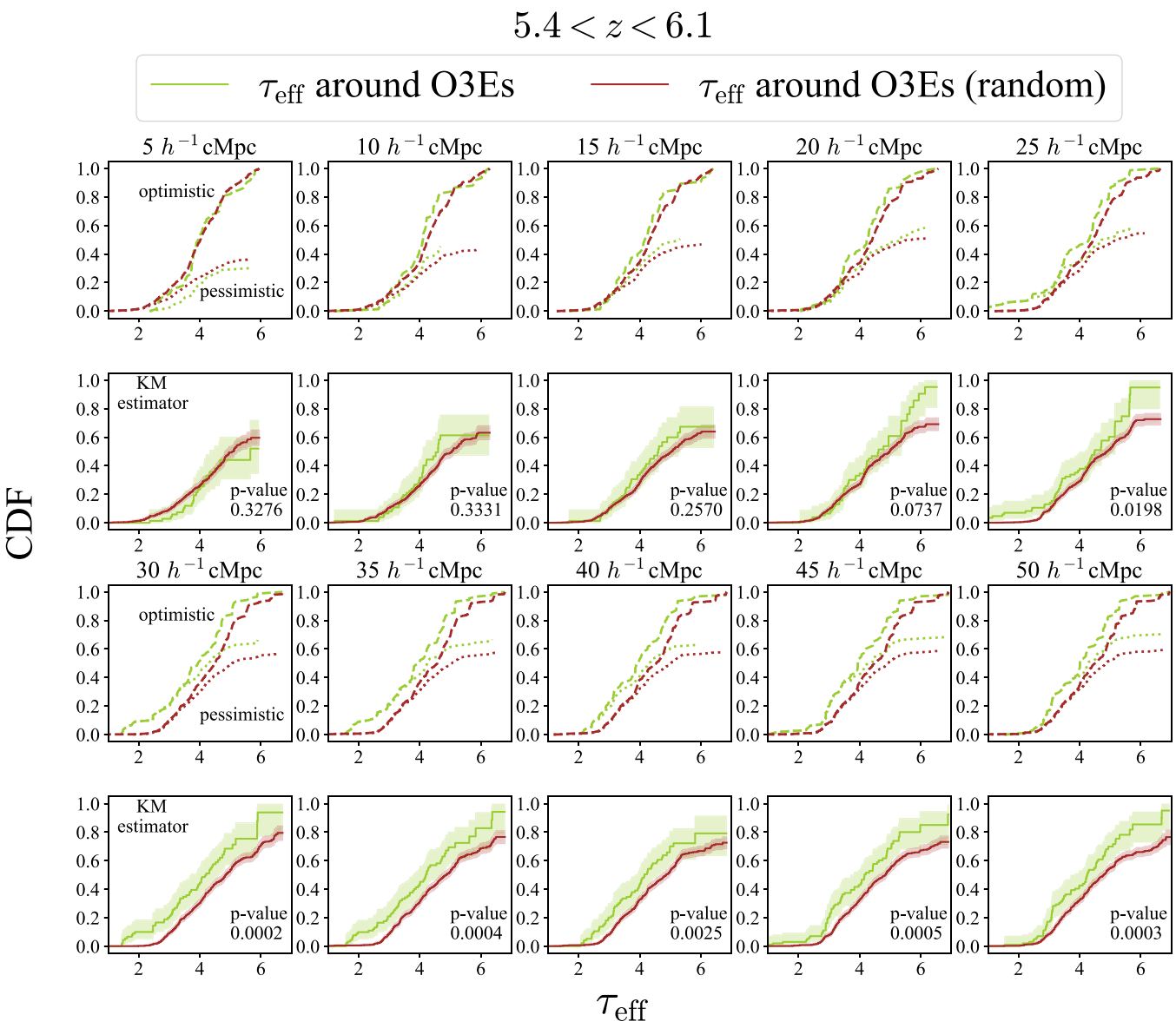


**Figure 9.** The first and the third rows show the CDFs of the $\tau_{\rm eff}$ around [O III] emitters at $5.4 < z < 6.1$ (yellow-green), adopting influence radii from 5 $h^{-1}$ cMpc to 50 $h^{-1}$ cMpc. The random cumulative distribution function of the $\tau_{\rm eff}$ around [O III] emitters is shown in brown, representing the $\tau_{\rm eff}$ distribution of IGM patches. The optimistic and the pessimistic CDFs are plotted in dashed and dotted lines, respectively. The second and the fourth rows show the fitted CDFs from the KM estimator and the $1\sigma$ confidence interval of the CDF is shown in the shaded regions of the corresponding color. The null hypothesis $p$-value from the log-rank test is shown in the bottom right corner of each subpanel. See the text for more details.

### 5.2. Redshift Evolution of IGM Effective Optical Depth Distribution around [O III] Emitters

To further investigate whether the $\tau_{\rm eff}$ distribution around [O III] emitters evolves with redshift, by adopting different influence radii, we study the CDFs of $\tau_{\rm eff,[O\ III]}$ in two different redshift bins: $5.7 < z < 6.1$ and $5.4 < z < 5.7$ in Figures 10 and 11. The selection of the redshift bins is motivated by: (1) D. Kashino et al. (2023) show the IGM-galaxy cross-correlation function signal can change with redshift from $z > 5.7$ to $z < 5.7$. An enhancement in IGM transmission than the average IGM transmission is observed at 5 cMpc from $5.7 < z < 6.14$ [O III] emitters, while around $5.3 < z < 5.7$ [O III] emitters, the IGM transmission is monotonically increasing with distance, up to the average IGM transmission; and (2) as shown in Figure 5, $\tau_{\rm eff,[O\ III]}$ measurements at $z > 5.7$ have nearly the same integrated length when measuring the effective optical depth around [O III] emitters. The nearly uniform integrated length will ensure a consistent scale when we compare the IGM transmission around [O III] emitters with the control sample.

#### 5.2.1. CDFs at $5.7 < z < 6.1$

Figure 10 shows the optimistic and pessimistic CDFs of $\tau_{\rm eff,[O\ III]}$ around $5.7 < z < 6.1$ [O III] emitters. We also use the KM estimator to fit the survival function of each distribution. The fitted CDF and the corresponding $1\sigma$ confidence interval are shown as the shaded region in Figure 10. Similar to the trend observed among all $z < 6.1$ $\tau_{\rm eff,[O\ III]}$ measurements, the fitted CDF of $\tau_{\rm eff,[O\ III]}$ is higher than the fitted random CDF at the same $\tau_{\rm eff,[O\ III]}$, suggesting the $\tau_{\rm eff}$ around [O III] emitters is generally lower. The most noticeable difference between the fitted CDFs appears at the right tail ($\tau_{\rm eff,[O\ III]}$>4) of the

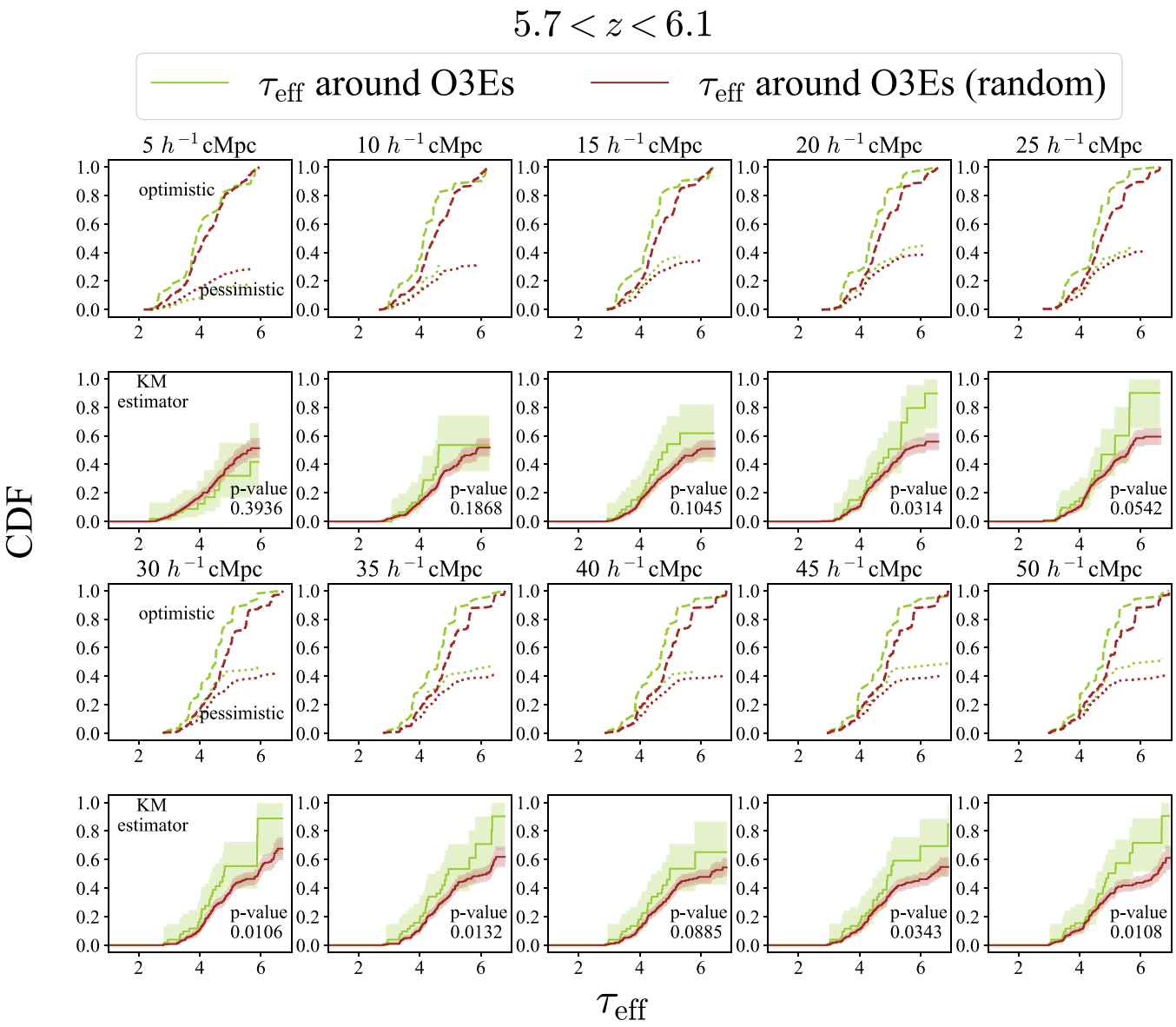


**Figure 10.** Similar to Figure 9, but for [O III] emitters at $5.7 < z < 6.1$.

distribution. The significant difference appears at a smaller scale (with an influence radius $\gtrsim 20\,h^{-1}$ cMpc) with a $p$-value $<0.05$ from the log-rank test and is not smeared out at large scales (an influence radius $\sim 50\,h^{-1}$ cMpc). This suggests that IGM patches are more transparent around [O III] emitters on scales $\gtrsim 20\,h^{-1}$ cMpc, implying ionizing photon contribution from [O III] emitters to the local ionizing background. Similar excess IGM transmission around $z \sim 6$ galaxies has been observed in K. Kakiichi et al. (2018), R. A. Meyer et al. (2019, 2020), and D. Kashino et al. (2023) by analyzing the IGM-galaxy cross-correlation function. K. Kakiichi et al. (2018) find an excess IGM transmission at $\sim 20$ cMpc from LBGs. R. A. Meyer et al. (2019) find an excess IGM transmission at $>10\,h^{-1}$ cMpc for faint galaxies traced by C IV absorbers and R. A. Meyer et al. (2020) report an excess IGM transmission at $>10$ cMpc around LBGs and LAEs. Using $5.7 < z < 6.14$ [O III] emitters, D. Kashino et al. (2023) find a peak of IGM transmission at $\sim 5$ cMpc. As these studies use various galaxy populations when measuring the IGM-galaxy cross-correlation function, the scales where the excess IGM transmission can be different due to different galaxy populations residing in different IGM environments (R. Momose et al. 2021). In addition, K. Kakiichi et al. (2018) and D. Kashino et al. (2023) measures the IGM-galaxy cross-correlation function in a single quasar field, therefore, the results can be subject to cosmic variance.

### 5.2.2. CDFs at $5.4 < z < 5.7$

Figure 11 shows the CDFs of $\tau_{\rm eff,[O\,III]}$ around $5.4 < z < 5.7$ [O III] emitters. With an influence radius of $5\,h^{-1}$ cMpc, the optimistic CDF of $\tau_{\rm eff,[O\,III]}$ shows a lower cumulative probability at the same $\tau_{\rm eff,[O\,III]}$ than the random distribution, indicating the IGM is more opaque close to $z < 5.7$ [O III] emitters within a scale of $5\,h^{-1}$ cMpc. However, from the KM estimator, the $1\sigma$ confidence intervals of two fitted CDFs overlap, and the $p$-value from the log-rank test is 0.33, indicating Ly$\alpha$ absorption near [O III] emitters is not significant, based on the current CDFs of $\tau_{\rm eff,[O\,III]}$. This can be caused by the large uncertainties in the fitted CDF, likely associated with the limited number of $z < 5.7$ $\tau_{\rm eff,[O\,III]}$

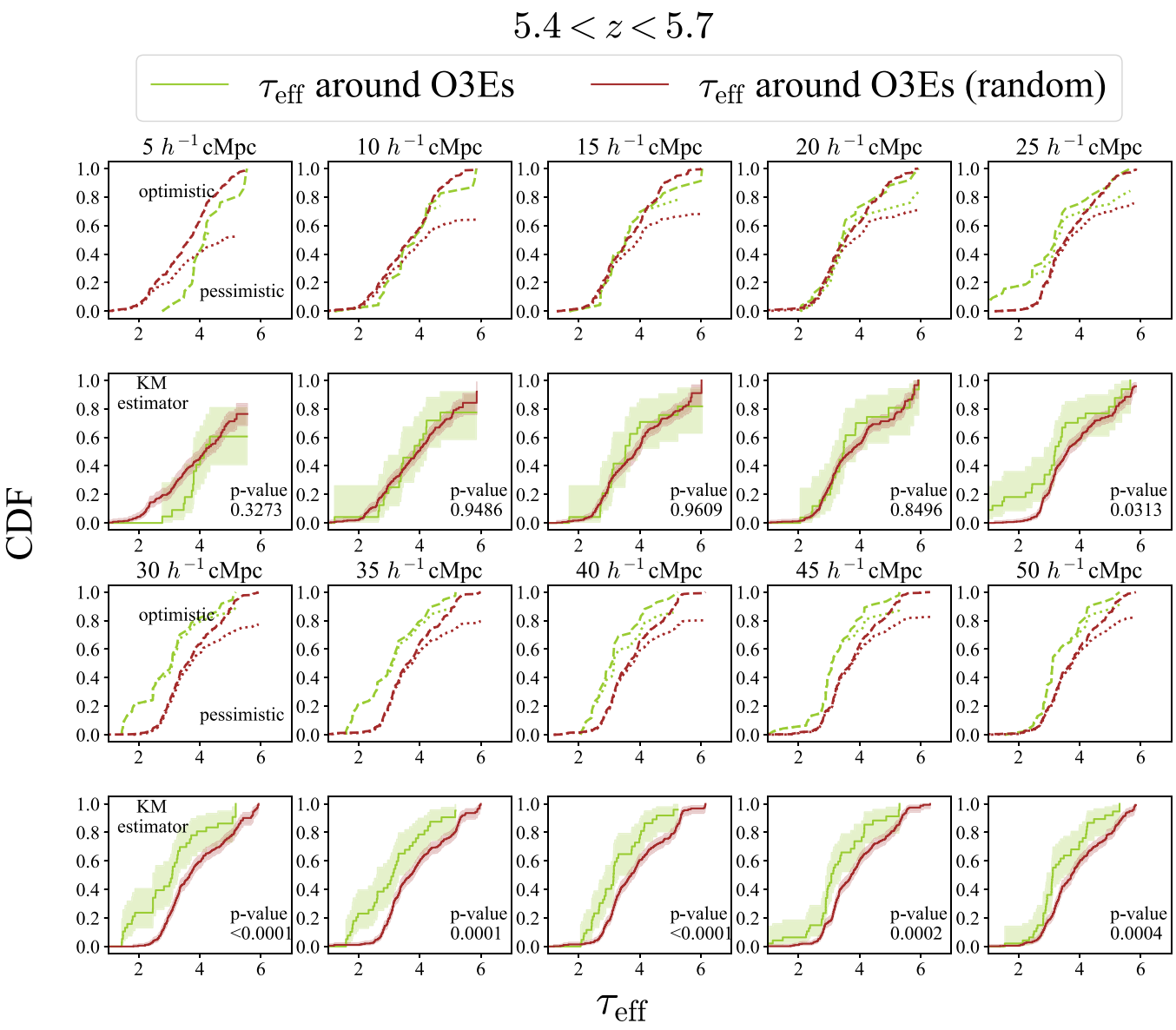


**Figure 11.** Similar to Figure 10, but for [O III] emitters at $5.4 < z < 5.7$.

measurements. Ly$\alpha$ absorption near galaxies has been observed in previous studies. By cross-correlating C IV absorbers at $4.5 < z < 6.2$ and Ly$\alpha$ forest, R. A. Meyer et al. (2019) find Ly$\alpha$ absorption within $5\,h^{-1}$ cMpc from C IV absorbers, indicating highly opaque regions surrounding faint galaxies traced by C IV absorbers. D. Kashino et al. (2023) measure the IGM-galaxy cross-correlation function through [O III] emitters and Ly$\alpha$ forest, and find IGM Ly$\alpha$ absorption within 8 cMpc from $5.3 < z < 5.7$ [O III] emitters. M. Tang et al. (2024) find that the Ly$\alpha$ profile of $z \sim 5-6$ strongest LAEs displays a typical redshifted Ly$\alpha$ velocity of 230 km s$^{-1}$ compared with H$\alpha$ emission line, and the Ly$\alpha$ profile does not show the blue Ly$\alpha$ peak as observed among $z \sim 2-3$ LAEs, suggesting the existence of residual H I around galaxies in the IGM absorbs the blue component of Ly$\alpha$ emission. At $z \sim 2-3$, similar Ly$\alpha$ forest absorption has also been found around several galaxy populations potentially due to H I overdensity around galaxies (e.g., R. Momose et al. 2021) or galaxy clusters (e.g., Z. Cai et al. 2017). At $z \sim 2-3$, S. Mukae et al. (2017) find a weak anticorrelation between the IGM transmission and galaxy overdensity within 2.5 proper Mpc. From the current CDFs of $\tau_{\rm eff,[O\,III]}$, Ly$\alpha$ absorption within $5\,h^{-1}$ cMpc from $z \sim 5.4-5.7$ [O III] emitters is not significant. More $z < 5.7$ $\tau_{\rm eff,[O\,III]}$ measurements will be needed to reconstruct the $\tau_{\rm eff,[O\,III]}$ distribution and to verify the existence of Ly$\alpha$ absorption near [O III] emitters within $5\,h^{-1}$ cMpc.

When adopting a larger influence radius than $5\,h^{-1}$ cMpc, the fitted CDF of $\tau_{\rm eff,[O\,III]}$ from the KM estimator first tends to be consistent with the fitted random CDF. However, with an influence radius $\gtrsim 25\,h^{-1}$ cMpc, the fitted CDF of $\tau_{\rm eff,[O\,III]}$ is higher than the fitted random CDF at the same $\tau_{\rm eff,[O\,III]}$, displaying a significant enhancement of IGM transmission around [O III] emitters on a larger scale $\gtrsim 25\,h^{-1}$ cMpc. The fitted CDF of $\tau_{\rm eff,[O\,III]}$ shows substantial divergence from the fitted random CDF at $\tau_{\rm eff,[O\,III]} \sim 3$. We further search the evidence of excess IGM transmission at $z < 5.7$ using existing WFSS programs in quasar fields, which fully cover a $5.4 < z < 5.7$ Ly$\alpha$ forest. In D. Kashino et al. (2023), the IGM-galaxy cross-correlation function beyond 15 cMpc is not available. By utilizing the published [O III] emitter catalog in

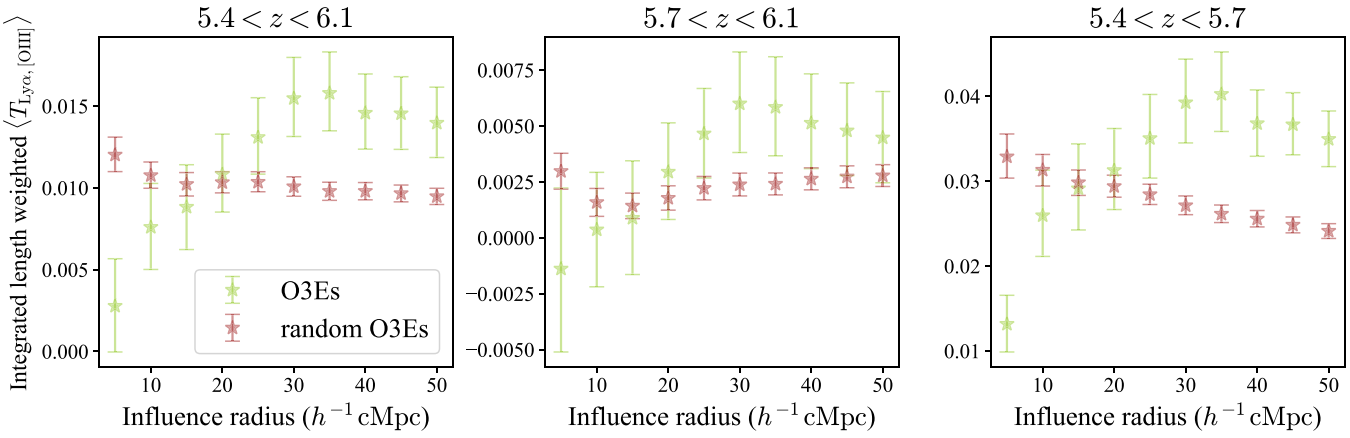


**Figure 12.** Average transmitted flux around [O III] emitters (filled yellow-green stars), weighted by the integrated length of each $\tau_{\rm eff,[O\ III]}$ measurement, as a function of influence radii at $5.4 < z < 6.1$, $5.7 < z < 6.1$, and $5.4 < z < 5.7$. The $1\sigma$ uncertainty is calculated using bootstrapping. The random values are denoted by filled brown stars.

D. Kashino et al. (2023) and the optical spectrum of SDSS J0100+2802 from the XQR-30 GitHub repository, we compute the IGM-galaxy cross-correlation function of $5.3 < z < 5.7$ [O III] emitters to a larger scale and find at $\sim$20 cMpc from $5.3 < z < 5.7$ [O III] emitters, there is also an enhanced IGM transmission compared with the average IGM transmission. However, since there is only one single quasar field, the result is greatly affected by cosmic variance.

For both the $5.7 < z < 6.1$ and $5.4 < z < 5.7$ bins, IGM transmission is observed to be higher around [O III] emitters on large scales. The significantly enhanced IGM transmission starts to appear at $\gtrsim 20\,h^{-1}$ cMpc around $z > 5.7$ [O III] emitters compared to the $\gtrsim 25\,h^{-1}$ cMpc scales of $z < 5.7$ [O III] emitters. The scales where the excess IGM transmission emerges are similar for both $z > 5.7$ and $z < 5.7$ [O III] emitters; however, the distinction between the fitted CDF of $\tau_{\rm eff,[O\ III]}$ and the fitted random CDF appears at $\tau_{\rm eff,[O\ III]} > 4$ for $z > 5.7$ [O III] emitters, while for $z < 5.7$ [O III] emitters, the fitted CDF of $\tau_{\rm eff,[O\ III]}$ already deviates from the fitted random CDF in the most transparent regime ($\tau_{\rm eff,[O\ III]} \lesssim 3$). This is related to the rapid redshift evolution of $\tau_{\rm eff}$ and a significant portion of $z > 5.7$ $\tau_{\rm eff,[O\ III]}$ are lower limits, resulting in large uncertainty in the fitted CDF. To better probe the excess IGM transmission around [O III] emitters at $z > 5.7$ and to further investigate whether the excess IGM transmission around [O III] emitters evolves with redshift, deep optical spectroscopy is needed (see also the discussion in Section 5.3).

It is worth noting that the scales around [O III] emitters where excess IGM transmission emerges should not be interpreted as the size of ionized bubbles directly (e.g., V. Tilvi et al. 2020; R. Endsley & D. P. Stark 2022; M. Tang et al. 2023; H. Umeda et al. 2023; L. Napolitano et al. 2024; M. Neyer et al. 2024; L. Whitler et al. 2024). Because $z \sim 6$ is close to the end of reionization, the majority of ionized regions in the IGM have largely overlapped in lieu of individually expanding in the significantly neutral IGM in the early stage of reionization. Beyond the scales around [O III] emitters where excess IGM transmission exhibits, the IGM is already ionized, not significantly neutral. Excess IGM transmission around [O III] emitters indicates the enhancement in the ionizing photons close to [O III] emitters within certain scales, compared with the average ionizing background (see also the discussion in X. Fan et al. 2006).

Because the field of view (FoV) of JWST NIRCam is small, it is plausible that our identification of IGM patches where no [O III] emitters are detected is not complete. Further [O III] emitters located at a transverse distance of $\gtrsim 6\,h^{-1}$ cMpc will not be covered by the existing single NIRCam pointing. In addition, the current depth of the ASPIRE program can only detect [O III] emitters down to a luminosity at $\sim 10^{42}$ erg s$^{-1}$. It is also likely that IGM patches where no [O III] emitters are detected can still have fainter, undetected [O III] emitters around them within the FoV of a single NIRCam pointing. A follow-up JWST program (PID: 3325, PIs: F. Wang and J. Yang) targets two ASPIRE quasars with a bigger mosaic ($\sim 4.'4 \times 7.'3$, corresponding to $7.4\,h^{-1}$ cMpc $\times$ $12.2\,h^{-1}$ cMpc at $z \sim 6$) and a deeper exposure around the quasar with NIRCam WFSS. We will use [O III] emitters selected from ASPIRE follow-up programs to test the influence of both the FoV and depth on our results.

### 5.3. Average Transmitted Flux around [O III] Emitters

In each distribution of $\tau_{\rm eff,[O\ III]}$, a subset of measurements are $2\sigma$ lower limits. In Sections 5.1 and 5.2, we adopt the KM estimator to fit the CDF of $\tau_{\rm eff,[O\ III]}$ and perform the log-rank test to investigate whether the IGM patches around [O III] emitters tend to be more transparent or more opaque than average IGM transmission. To verify whether the results are subject to the fact that $2\sigma$ lower limits of $\tau_{\rm eff,[O\ III]}$ are included in the distribution, we calculate the average transmitted flux in the distribution, and explore whether there is excess IGM transmission compared with the random distribution, which represents a baseline of IGM transmission. For each distribution in Figures 9, 10, and 11, we calculate its average transmitted flux when adopting a certain influence radius, weighted by the integrated length for each measurement, and derive the $1\sigma$ uncertainty in the average transmitted flux by bootstrapping. Figure 12 shows the average transmitted flux around [O III] emitters as a function of influence radii in three redshift ranges: $5.4 < z < 6.1$, $5.7 < z < 6.1$, and $5.4 < z < 5.7$. It is important to note that Figure 12 is different than the average transmitted flux as a function of distance to galaxies (i.e., $T(r)$, see K. Kakiichi et al. 2018; R. A. Meyer et al. 2019, 2020; D. Kashino et al. 2023) because we calculate the average transmitted flux over the integrated length by adopting

an influence radius, instead of at a certain distance from galaxies.

At $5.4 < z < 6.1$, the transmitted flux around [O III] emitters tends to be lower than the random distribution with an influence radius of $5\,h^{-1}$ cMpc. Compared with the random distribution, the excess in transmitted flux around [O III] emitters starts to appear with influence radii $\gtrsim 25\,h^{-1}$ cMpc, and the excess in transmitted flux becomes more significant ($\sim 2\sigma$) adopting an influence radius $\gtrsim 30\,h^{-1}$ cMpc. The $25\,h^{-1}$ cMpc influence radius where the excess IGM transmission appears is consistent with the influence radius where the fitted CDF of $\tau_{\rm eff,[O\ III]}$ is significantly different from the random distribution shown in Figure 9.

As for the $5.7 < z < 6.1$ bin, with an influence radius of $\lesssim 20\,h^{-1}$ cMpc, the average transmitted flux around [O III] emitters and the random transmitted flux overlap with each other within $1\sigma$ uncertainty. Excess in transmitted flux around [O III] emitters exists when adopting influence radii $\gtrsim 25\,h^{-1}$ cMpc. Such excess is most evident when adopting an influence radius of $\sim 30-35\,h^{-1}$ cMpc, but the significance of the excess in transmitted flux is less than $2\sigma$. Because the transmitted flux in the Ly$\alpha$ forest is low at $z \sim 6$, it is challenging to constrain the transmitted flux precisely, especially using shallow spectroscopy. Therefore, the significance of excess transmission can be underestimated because noisy spectra can dilute the signal of excess transmission.

For the $5.4 < z < 5.7$ bin, with an influence radius of $5\,h^{-1}$ cMpc, the average transmitted flux around [O III] emitters is significantly lower ($\sim 4.7\sigma$) than the random value. However, the fitted CDF of $\tau_{\rm eff,[O\ III]}$ from the KM estimator does not differ significantly from the random CDF when adopting an influence radius of $5\,h^{-1}$ cMpc because of the large uncertainty in the fitted CDF. When increasing the influence radii to $\gtrsim 25\,h^{-1}$ cMpc, the average transmitted flux around [O III] emitters becomes higher than the random average transmitted flux. The excess in transmitted flux around [O III] emitters is most significant ($\sim 3.1\sigma$) when adopting an influence radii of $\sim 30-50\,h^{-1}$ cMpc. The scales showing Ly$\alpha$ excess Ly$\alpha$ transmission are consistent with the scales where the fitted CDF of $\tau_{\rm eff,[O\ III]}$ is significantly different than the random distribution in Figure 11.

To summarize, we find that the scales exhibiting lower or higher transmitted flux around [O III] emitters are mostly consistent with those where the fitted $\tau_{\rm eff,[O\ III]}$ distribution from the KM estimator deviates significantly from the fitted random distribution. When investigating the transmission around [O III] emitters, both the average transmitted flux and the $\tau_{\rm eff,[O\ III]}$ distribution exhibit their own advantages and limitations. Using the average transmitted flux around [O III] emitters, it is straightforward to determine whether the transmission is enhanced or suppressed around [O III] emitters, compared with the average IGM transmission. On the other hand, for $\tau_{\rm eff,[O\ III]}$ measurements, a substantial sample size is required to reconstruct the distribution and thus to investigate transmission around [O III] emitters. However, average transmitted flux can be biased toward high transmitted flux. Because the average IGM transmitted flux decreases substantially as the redshift increases (G. D. Becker et al. 2015; S. E. I. Bosman et al. 2018, 2022; A.-C. Eilers et al. 2018; J. Yang et al. 2020b), the average transmitted flux within a broad redshift range will be naturally biased toward lower redshift, while $\tau_{\rm eff,[O\ III]}$ measurements can demonstrate the entire distribution of IGM transmission. Nevertheless, both methods can be limited by noisy spectra. Using noisy data, it is difficult to measure the transmitted flux precisely, and there are also more lower limits in the $\tau_{\rm eff,[O\ III]}$ distribution, resulting in a large uncertainty in the fitted CDF.

Recent ionizing photon mean free path ($\lambda_{\rm mfp}$) measurements show the rapid evolution of $\lambda_{\rm mfp} = 0.81^{+0.73}_{-0.48}$ pMpc at $z = 5.93$ to $\lambda_{\rm mfp} = 3.31^{+2.74}_{-1.34}$ pMpc at $z = 5.65$ (Y. Zhu et al. 2023, see also G. D. Becker et al. 2018; P. Gaikwad et al. 2023; F. B. Davies et al. 2024). In the scenario where the scatter in $\tau_{\rm eff}$ is primarily driven by ionizing background fluctuations, the fluctuations in the Ly$\alpha$ forest are stronger with a shorter $\lambda_{\rm mfp}$ (F. B. Davies et al. 2024). As such, the excess transmission around [O III] emitters might show a redshift evolution when the scatter in $\tau_{\rm eff}$ is dominated by the ionizing background fluctuations. However, due to the moderate depth of data, currently, we do not find conclusive evidence of the redshift evolution of excess transmission around [O III] emitters.

This emphasizes the necessity for deeper exposure and more quasar sightlines for quasar optical spectroscopy, especially to detect weak transmission at $z \sim 6$, in order to investigate the redshift evolution of the excess IGM transmission around [O III] emitters.

## 6. Summary

In this paper, we present the first $\tau_{\rm eff}$ measurements around [O III] emitters at $5.4 < z < 6.1$ identified in 14 fields of the ASPIRE program centered on $z \sim 6.5-6.8$ quasars for which we have a good quality spectrum. We find:

1. By stacking the Ly$\alpha$ transmission around [O III] emitters with an influence radius of $25\,h^{-1}$ cMpc, we find at the same redshift, IGM patches around [O III] emitters are significantly more transparent ($d\tau_{\rm eff} > 0.5$) than those IGM patches where no [O III] emitters are detected. At $z > 5.7$, most IGM transmission is within $25\,h^{-1}$ cMpc from [O III] emitters, reinforcing the important roles of galaxies in producing IGM transmission as observed in the Ly$\alpha$ forest.
2. Stacked IGM patches around [O III] emitters reach the same optical depth at least $dz \sim 0.1$ ahead of stacked IGM patches away from [O III] emitters, supporting earlier reionization around [O III] emitters.
3. With an influence radius $\gtrsim 25\,h^{-1}$ cMpc, we find that the $\tau_{\rm eff}$ distribution around $5.4 < z < 6.1$ [O III] emitters is significantly different from the IGM $\tau_{\rm eff}$ distribution, and the average transmitted flux around [O III] emitters is higher than the average IGM transmitted flux, supporting that the scatter in the observed $z > 5.5$ $\tau_{\rm eff}$ is tightly associated with the large-scale fluctuations in the ionizing background. By splitting all [O III] emitters into two redshift bins, $5.4 < z < 5.7$ and $5.7 < z < 6.1$, we find the scales where the excess IGM transmission emerges are similar for $5.4 < z < 5.7$ ($\gtrsim 25\,h^{-1}$ cMpc) and $5.7 < z < 6.1$ ($\gtrsim 20\,h^{-1}$ cMpc) bins. Deeper optical spectroscopy will be needed to further investigate the redshift evolution of excess transmission around [O III] emitters.

We have ongoing programs on 6–10 m ground-based telescopes to collect the optical spectroscopy of ASPIRE quasars to complete the ASPIRE sample and also to increase the S/N of the existing optical quasar spectroscopy. The IGM-

galaxy connection studies of the full ASPIRE quasar sample will be presented in later works.

## Acknowledgments

We thank the anonymous reviewer for constructive comments that improved this manuscript. X.J. thanks Yongda Zhu, Daichi Kashino, and Andrei Mesinger for the informative discussions. F.W. acknowledges support from NSF Grant AST-2308258. R.A.M. acknowledges support from the Swiss National Science Foundation (SNSF) through project grant 200020_207349. G.D.B. was supported by the NSF through grant AST-1751404. S.Z. acknowledges support from the National Science Foundation of China (grant No. 12303011).

This work is based on observations made with the NASA/ESA/CSA JWST. The data were obtained from the Mikulski Archive for Space Telescopes at the Space Telescope Science Institute, which is operated by the Association of Universities for Research in Astronomy, Inc., under NASA contract NAS 5-03127 for JWST. The specific observations analyzed can be accessed via doi:10.17909/vt74-kd84. These observations are associated with program #2078. Support for program #2078 was provided by NASA through a grant from the Space Telescope Science Institute, which is operated by the Association of Universities for Research in Astronomy, Inc., under NASA contract NAS 5-03127.

This work is based in part on observations made with ESO telescopes at the La Silla Paranal Observatory under program IDs 087.A-0890(A), 088.A-0897(A), 097.B-1070(A), 098.A-0444(A), 098.B-0537(A), 0100.A-0625(A), 0102.A-0154(A), 1103.A-0817(A), 1103.A-0817(B), and 2102.A-5042(A). The paper also used data based on observations obtained at the international Gemini Observatory, a program of NSF's NOIRLab, which is managed by the Association of Universities for Research in Astronomy (AURA) under a cooperative agreement with the National Science Foundation on behalf of the Gemini Observatory partnership: the National Science Foundation (United States), National Research Council (Canada), Agencia Nacional de Investigación y Desarrollo (Chile), Ministerio de Ciencia, Tecnología e Innovación (Argentina), Ministério da Ciência, Tecnologia, Inovações e Comunicações (Brazil), and Korea Astronomy and Space Science Institute (Republic of Korea). This paper includes data gathered with the 6.5 m Magellan telescopes located at Las Campanas Observatory, Chile. Some of the data presented herein were obtained at the W. M. Keck Observatory, which is operated as a scientific partnership among the California Institute of Technology, the University of California and the National Aeronautics and Space Administration. The Observatory was made possible by the generous financial support of the W. M. Keck Foundation.

The authors wish to recognize and acknowledge the very significant cultural role and reverence that the summit of Maunakea has always had within the indigenous Hawaiian community. We are most fortunate to have had the opportunity to conduct observations from this mountain.

We respectfully acknowledge the University of Arizona is on the land and territories of Indigenous peoples. Today, Arizona is home to 22 federally recognized tribes, with Tucson being home to the O'odham and the Yaqui. Committed to diversity and inclusion, the University strives to build sustainable relationships with sovereign Native Nations and Indigenous communities through education offerings, partnerships, and community service.

*Facilities:* JWST, VLT:Kueyen (X-Shooter), Gemini:South (GMOS), Keck:I (LRIS), Keck:II (DEIMOS), Magellan:Clay (LDSS3).

*Software:* astropy (Astropy Collaboration et al. 2013, 2018, 2022), NumPy (C. R. Harris et al. 2020), Matplotlib (J. D. Hunter 2007), PypeIt (J. Prochaska et al. 2020a; J. X. Prochaska et al. 2020b), SciPy (P. Virtanen et al. 2020).

## Appendix A
## Quasar Sightline Plots

In this appendix, we show the transmitted spectrum of all ASPIRE quasar sightlines used in this work and the spatial location of [O III] emitters identified in the quasar fields in Figures 13–16.

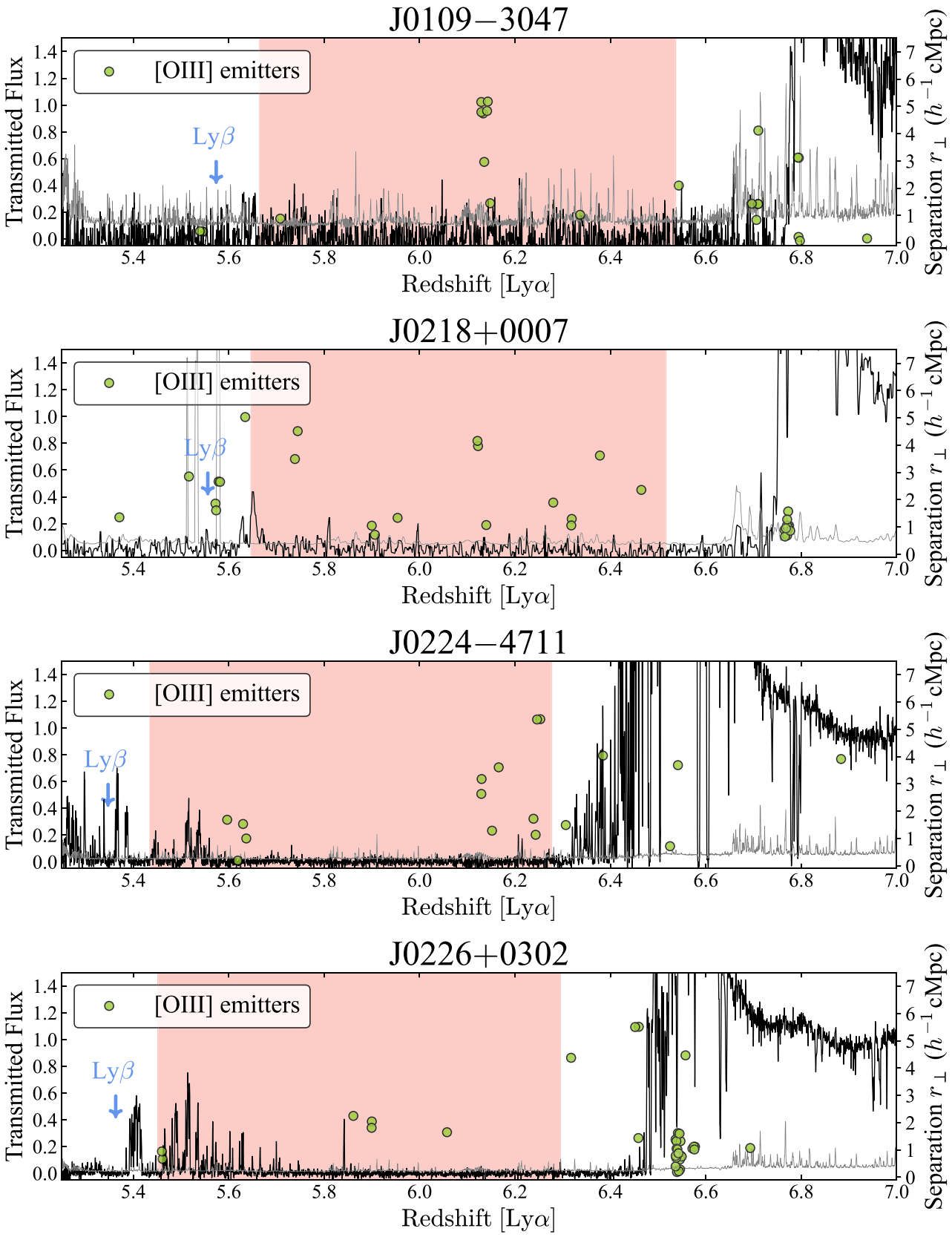


**Figure 13.** The transmitted spectrum of all quasars used in this work, in the ascending order of R.A. The transmitted spectrum (black) has been smoothed with a median filter for better visualization. The spectral uncertainty is shown in gray. The redshift range of the Ly$\alpha$ used in the analysis is displayed in the red-shaded region. The location of the Ly$\beta$ emission line is marked by the blue downward arrow. The spatial locations of the [O III] emitters identified in each quasar field are denoted by the yellow-green circles in terms of the [O III] emitter redshift $z_{[\mathrm{O\ III}]}$ and the transverse distance $r_\perp$ between the [O III] emitter and the central quasar.

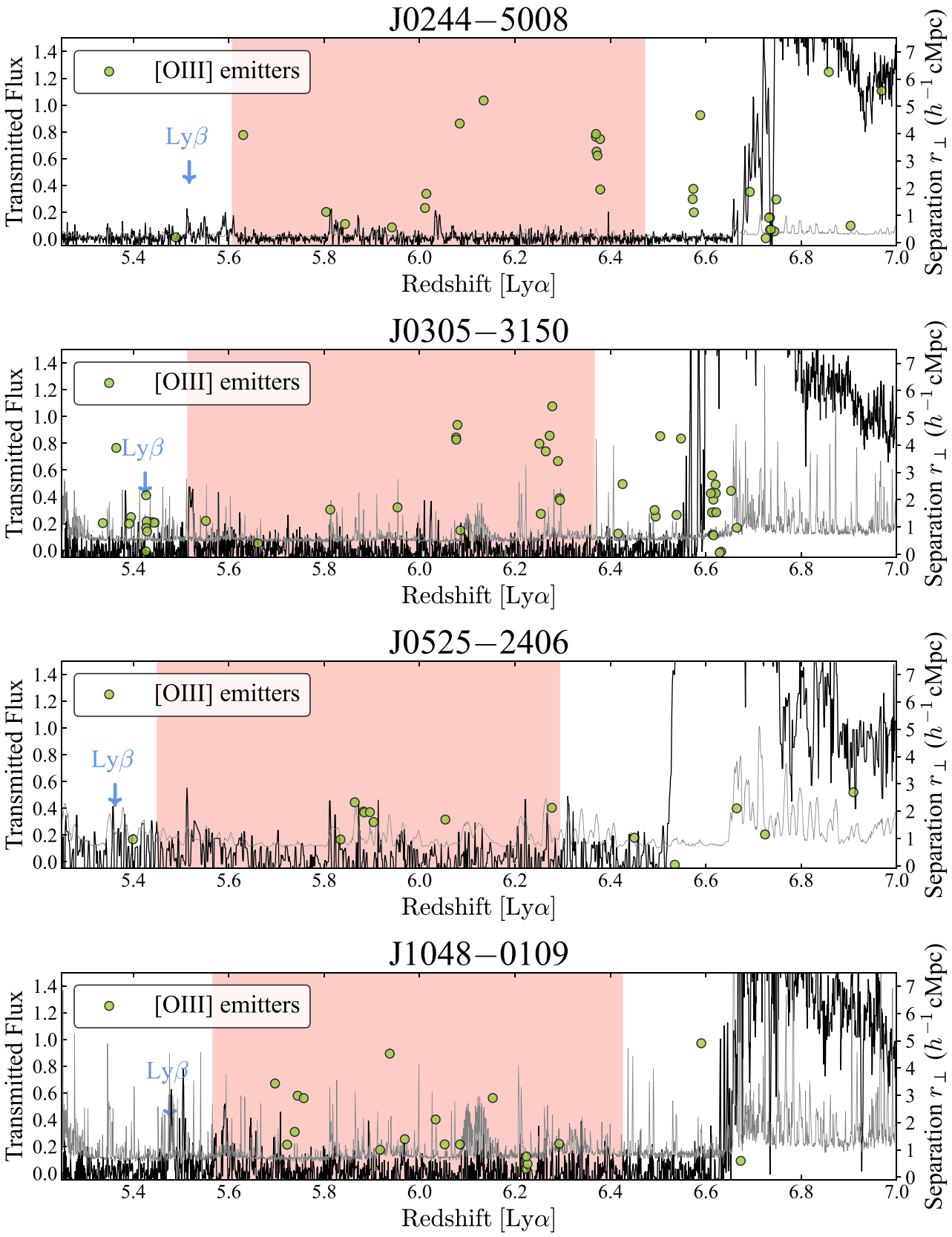


**Figure 14.** (continued.) The transmitted spectrum of ASPIRE quasars J0244+5008, J0305−3150, J0525−2406, and J1048−0109, together with [O III] emitters detected in the quasar fields.

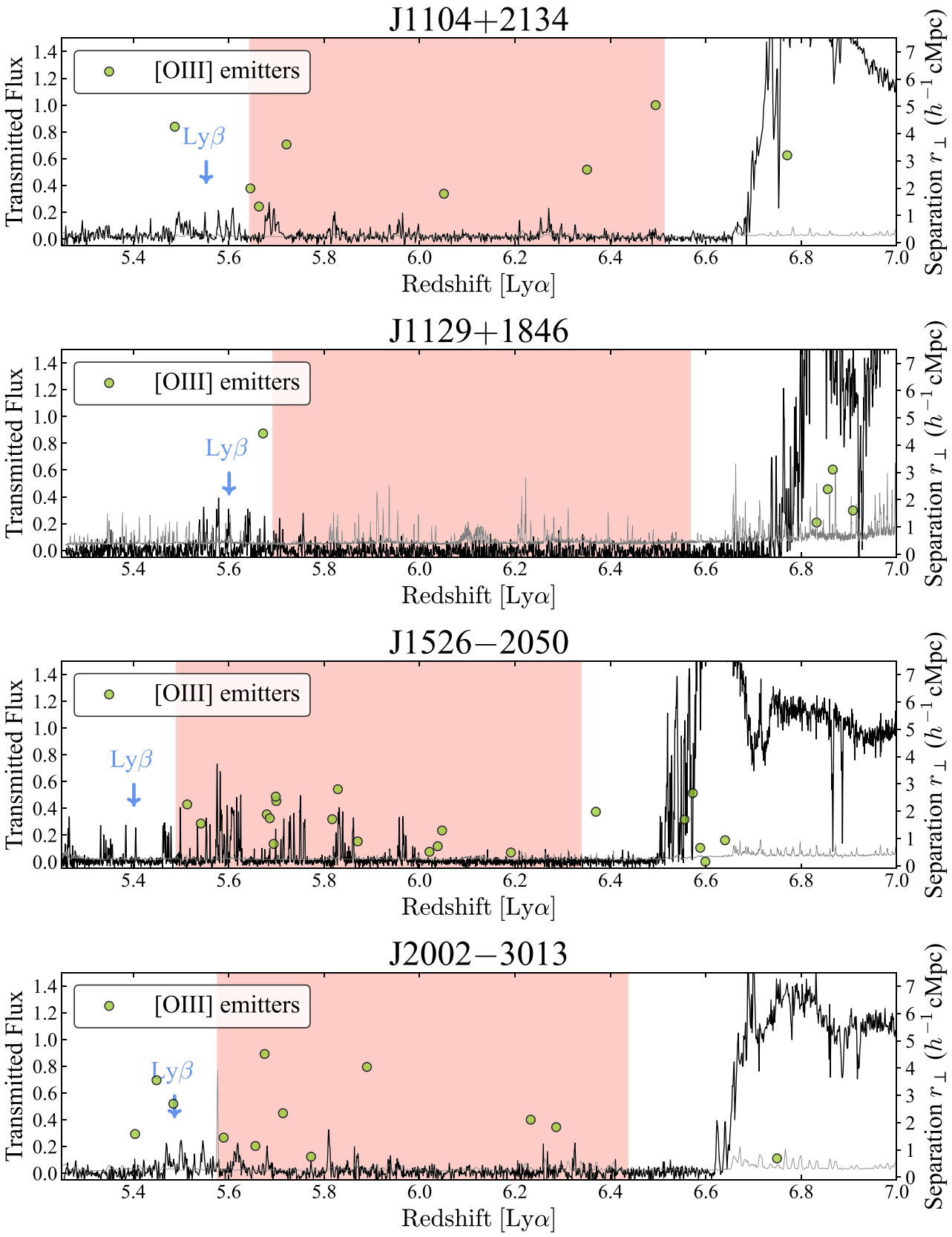


**Figure 15.** (continued.) The LOS plot of ASPIRE quasars J1104+2134, J1129+1846, J1526−2050, and J2002−3013, together with [O III] emitters detected in the quasar fields.

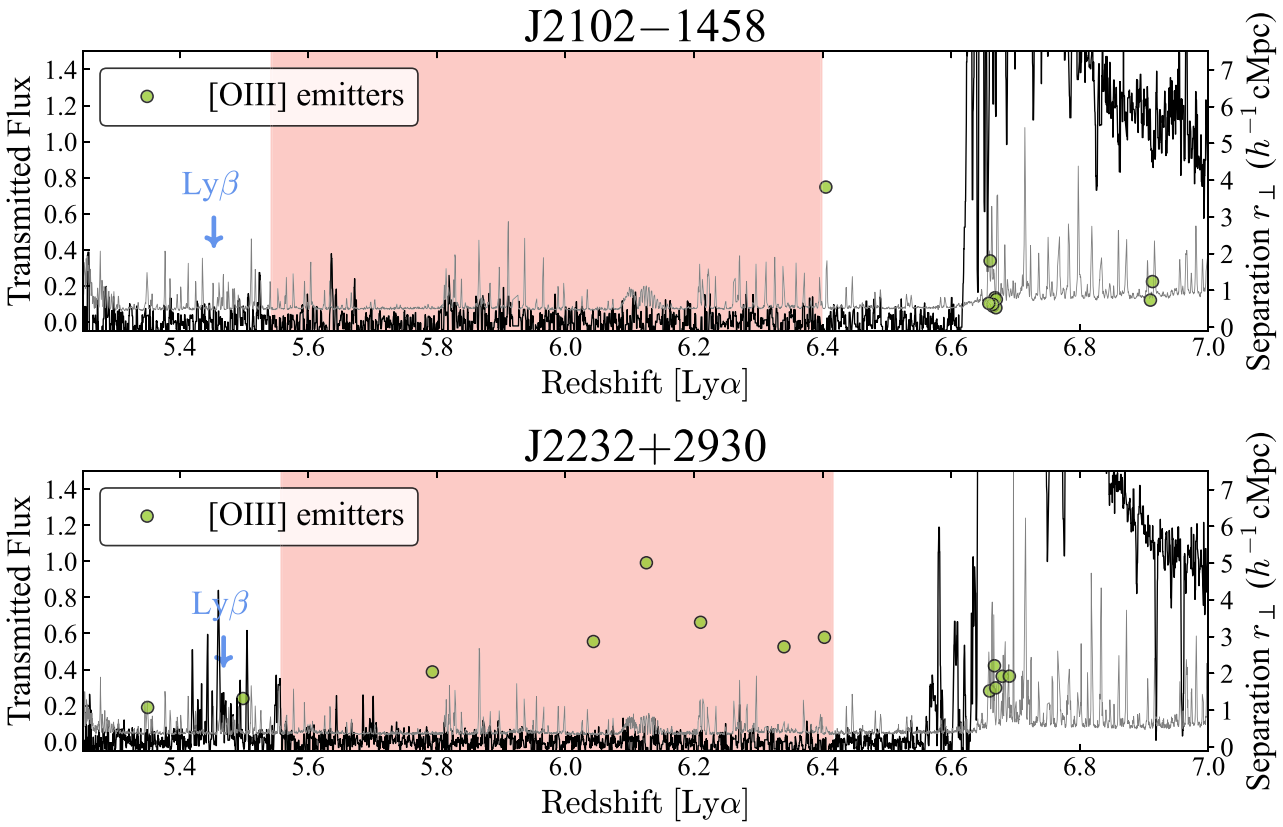


**Figure 16.** (continued.) The LOS plot of ASPIRE quasars J2102−1458 and J2232+2930, together with [O III] emitters detected in the quasar fields.

## Appendix B
## Consistency Check between the Random $\tau_{\rm eff,[O\ III]}$ Distribution and the IGM Effective Optical Depth Distribution

In this appendix, we investigate whether the random distribution of $\tau_{\rm eff}$ around [O III] emitters ($\tau_{\rm eff,[O\ III]}$) can recover the $\tau_{\rm eff}$ distribution $\tau_{\rm eff}$ of IGM patches at the corresponding redshifts. For the Ly$\alpha$ forest spectrum of each quasar, we use the spatial locations (redshift and transverse distance) of [O III] emitters detected in the other 13 quasar fields to compute the random $\tau_{\rm eff,[O\ III]}$, following the method described in Section 3. For each influence radius, we use twice the influence radius as the bin size to calculate the $\tau_{\rm eff}$ of IGM patches, starting from the rest frame 1040 Å up to the rest frame 1176 Å in the quasar Ly$\alpha$ forest.

We plot the optimistic CDFs of random $\tau_{\rm eff,[O\ III]}$ distribution and the $\tau_{\rm eff}$ distribution of IGM patches in brown and black dashed lines. The corresponding pessimistic CDFs are denoted by the dotted lines. We then use the KM estimator to fit the survival function of each distribution. We show the fitted CDFs and 1$\sigma$ confidence intervals of random $\tau_{\rm eff,[O\ III]}$ distribution and $\tau_{\rm eff}$ distribution of IGM patches by brown and black solid lines and shaded regions in Figure 17 ($5.4 < z < 6.1$), Figure 18 ($5.7 < z < 6.1$), and Figure 19 ($5.4 < z < 5.7$), respectively. We perform the log-rank test between these two distributions, and the $p$-values for the null hypothesis are greater than 0.05 for any influence radius in all three redshift bins, indicating the random $\tau_{\rm eff,[O\ III]}$ distribution is consistent with the $\tau_{\rm eff}$ distribution of IGM patches. As such, the random $\tau_{\rm eff,[O\ III]}$ distribution can well represent the $\tau_{\rm eff}$ distribution of IGM patches at the corresponding redshifts.

At $\tau_{\rm eff} \lesssim 3$ in both $5.4 < z < 6.1$ and $5.4 < z < 5.7$ bins, the random $\tau_{\rm eff,[O\ III]}$ distribution tends to have a more extended low $\tau_{\rm eff}$ tail than the $\tau_{\rm eff}$ distribution of IGM patches. This is due to the fact that our method for measuring the $\tau_{\rm eff,[O\ III]}$ can include [O III] emitters with redshift less than the low-redshift cut of the Ly$\alpha$ forest, as long as the [O III] emitters can enclose part of the Ly$\alpha$ forest spectrum within the influence radius. Equivalently, $\tau_{\rm eff,[O\ III]}$ include the spectrum close to the boundary of the Ly$\alpha$ forest, while the $\tau_{\rm eff}$ distribution of IGM patches is calculated within a large bin size with a midpoint redshift slightly higher than the low-redshift boundary of the Ly$\alpha$ forest. As the $\tau_{\rm eff}$ increases with redshift, the $\tau_{\rm eff} < 3$ cannot be well sampled by the $\tau_{\rm eff}$ distribution of IGM patches.

Furthermore, because the number of quasar sightlines is only 14, the number of IGM patches is very limited when adopting a large bin size to calculate $\tau_{\rm eff}$. This effect becomes more obvious at $5.4 < z < 5.7$ than at $5.7 < z < 6.1$ since not every quasar sightline fully covers the Ly$\alpha$ forest at $5.4 < z < 5.7$. Therefore, we use the random $\tau_{\rm eff,[O\ III]}$ distribution as the control sample for the IGM transmission to compare with the $\tau_{\rm eff,[O\ III]}$ distribution.

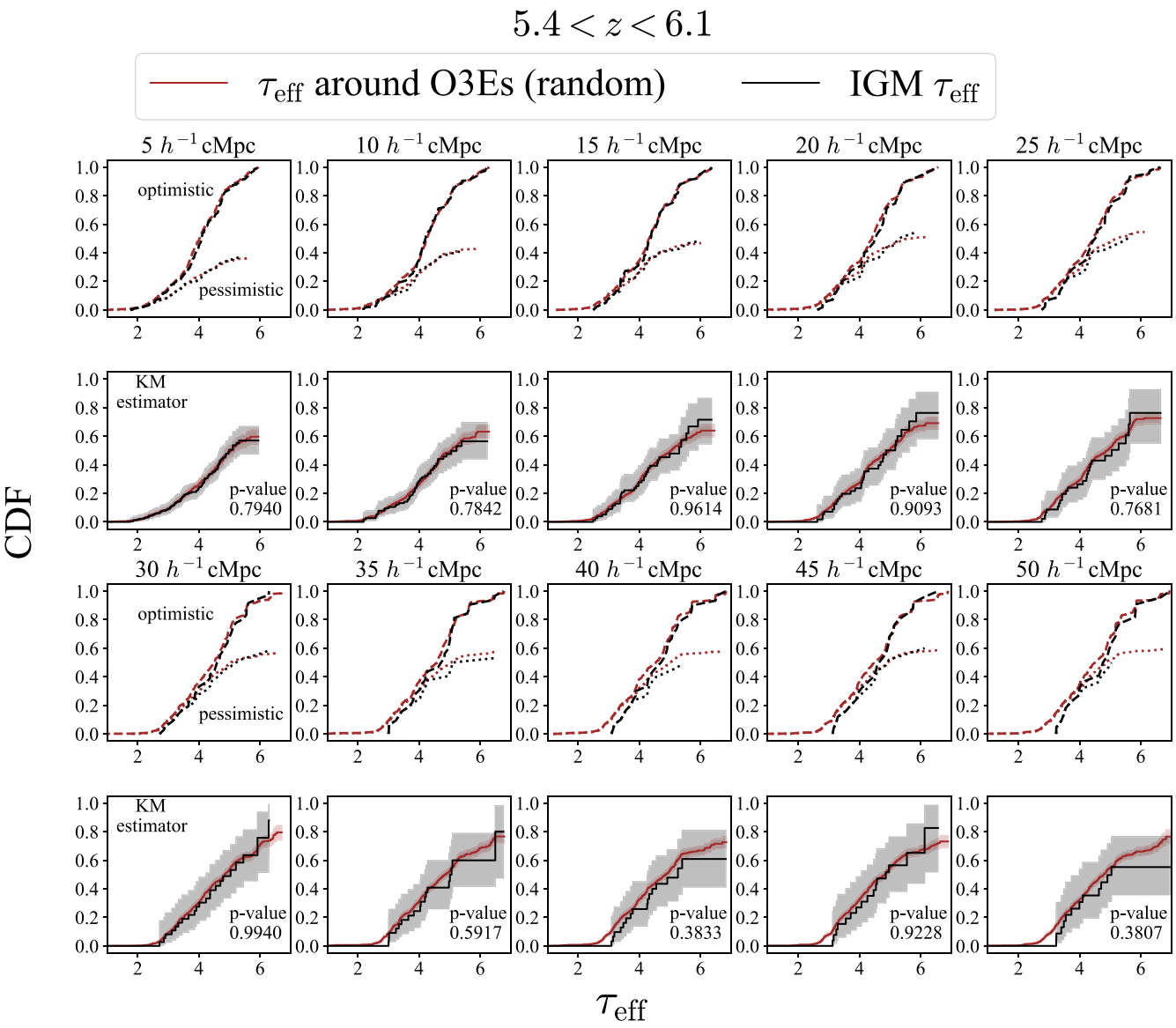


**Figure 17.** The first and the third rows show the CDFs of the random $\tau_{\rm eff}$ around [O III] emitters (brown) and $\tau_{\rm eff}$ of IGM patches (black) at $5.4 < z < 6.1$. The influence radius is from 5 $h^{-1}$ cMpc to 50 $h^{-1}$ cMpc for $\tau_{\rm eff,[O\ III]}$ measurements and $\tau_{\rm eff}$ are measured using the bin size of twice the corresponding influence radius. The optimistic and the pessimistic CDFs are plotted in dashed and dotted lines, respectively. The second and the fourth rows show the fitted CDFs from the KM estimator and the $1\sigma$ confidence interval of the CDF is shown in the shaded regions of the corresponding color. The null hypothesis $p$-value from the log-rank test is shown in the bottom right corner of each subpanel. With all influence radii, the random $\tau_{\rm eff,[O\ III]}$ distribution is consistent with the $\tau_{\rm eff}$ distribution of IGM patches.

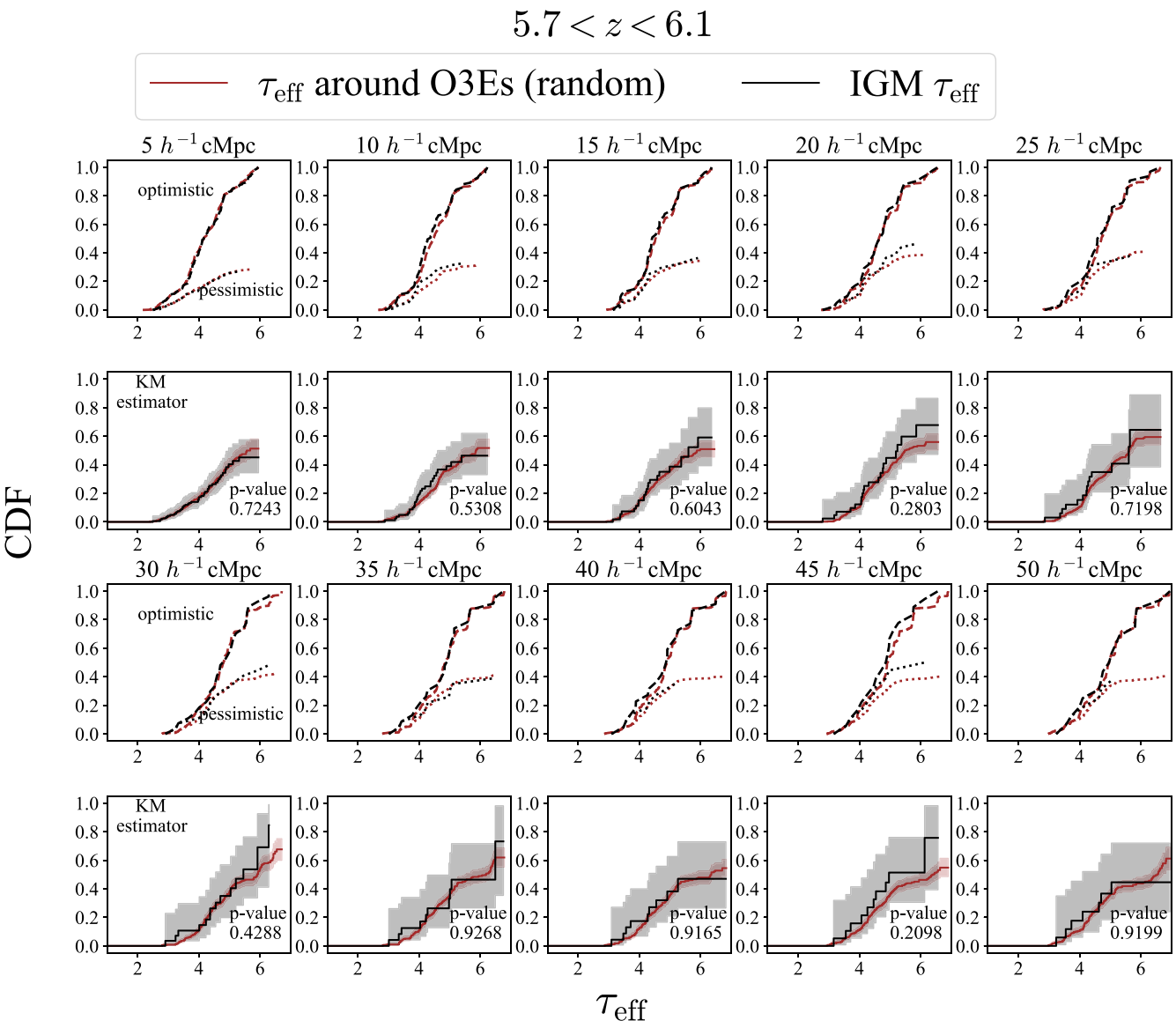


**Figure 18.** The CDF of the random $\tau_{\rm eff,[O\ III]}$ (brown) and $\tau_{\rm eff}$ of IGM patches (black) at $5.7 < z < 6.1$.